PHYSICAL REVIEW E **90**, 053004 (2014)

Chemical convection in the methylene-blue–glucose system: Optimal perturbations and three-dimensional simulations

Thomas Köllner,[1,*] Maurice Rossi,[2] Frauke Broer,[1] and Thomas Boeck[1]
[1]*Insitute of Thermodynamics and Fluid Mechanics, TU Ilmenau, P. O. Box 100565, 98684 Ilmenau, Germany*
[2]*CNRS, UMR 7190, UPMC Université Paris 06, Institut Jean Le Rond d'Alembert, Paris F-75005, France*

(Received 4 July 2014; published 7 November 2014)

A case of convection driven by chemical reactions is studied by linear stability theory and direct numerical simulations. In a plane aqueous layer of glucose, the methylene-blue-enabled catalytic oxidation of glucose produces heavier gluconic acid. As the oxygen is supplied through the top surface, the production of gluconic acid leads to an overturning instability. Our results complement earlier experimental and numerical work by Pons *et al.* First, we extend the model by including the top air layer with diffusive transport and Henry's law for the oxygen concentration at the interface to provide a more realistic oxygen boundary condition. Second, a linear stability analysis of the diffusive basic state in the layers is performed using an optimal perturbation approach. This method is appropriate for the unsteady basic state and determines the onset time of convection and the associated wavelength. Third, the nonlinear evolution is studied by the use of three-dimensional numerical simulations. Three typical parameters sets are explored in detail showing significant differences in pattern formation. One parameter set for which the flow is dominated by viscous forces, displays persistently growing convection cells. The other set with increased reaction rate displays a different flow regime marked by local chaotic plume emission. The simulated patterns are then compared to experimental observations.

DOI: 10.1103/PhysRevE.90.053004 PACS number(s): 47.55.P−, 47.54.−r, 47.70.Fw, 47.20.−k

I. INTRODUCTION

Mass transport in fluids coupled to chemical reactions is central to many processes in nature [1], chemical engineering [2], and geoengineering [3]. Convection and thereby mass transport can be triggered due to density gradients (Rayleigh-Bénard convection [4]), and/or to gradients in surface tension (Marangoni convection [5]). The coupling of these forces and gradients in chemical composition lead to complex dynamical behaviors actively studied in the field of chemohydrodynamics [6]. Paradigmatic theoretical or experimental studies of chemohydrodynamic effects have focused on configurations that are initially quiescent and spatially heterogeneous in composition. In these systems, chemical reactions can take place in one phase (single liquid phase) or in two phases (immiscible liquid-liquid layers, gas-liquid phases).

One-phase systems have been studied with initial compositional gradients parallel or perpendicular to gravity. For compositional gradients parallel to gravity, let us mention the acid-base reaction with convection due to density effects [7–10], autocatalytic fronts [11,12], and, recently, oscillating chemical reactions [13]. For a compositional gradient perpendicular to gravity, different reaction schemes have been studied with buoyancy effects [14] as well as Marangoni effects occurring at an interface with another physical domain (e.g., an air layer) which is not involved in the chemical process [15,16]. Note that when a reaction product is volatile and therefore migrating in the other domain, as observed in the iodate-arsenous acid reaction [17], the situation may be described as a two-phase system.

Typical two-phase systems are immiscible liquid-liquid layers, e.g., immiscible solvent phases that are stably stratified with a compositional gradient in the direction of gravity due to phase specific solute loading. For two-phase systems, the presence of an interface leads to several new consequences: hindrance of species advection through the interface, interfacial forces, differential solubility, and phase changes to name only a few.

Often chemical reactions preferentially occur at the interface causing Marangoni and Rayleigh-Bénard instabilities [18–21]. One observes more variability in the possible dynamical behaviors than for one-phase systems. An even more complex situation is the presence of partially miscible phases. Recently, the dissolution of alky formates in water with their subsequent hydrolysis has been studied [22]. In such situations, the Marangoni and Rayleigh-Bénard convection can be tuned by dissolution of additional acids or bases.

Due to the experimental accessibility, numerous experiments and related simulations in the field of chemohydrodynamics[1] have been done in a Hele-Shaw (HS) setup [18]: two plates separated by a thin gap, which are able to enforce a mostly two-dimensional situation. For instance, all the works referenced above were concerned with these approximately two-dimensional experimental or numerical situations. Truly three-dimensional cases have been considered experimentally in photochemical reactions near interfaces [23,24] or reactions due to gas transfer [25]. An overview of experimental work for systems with photochemical and mass transfer showing density-gradient-driven convection can be found in [26].

Numerical analysis of chemohydrodynamic pattern formation have been rarely performed in a fully three-dimensional context. In the present work, it is our purpose to study numerically the full three-dimensional pattern formation process,

---

[*] thomas.koellner@tu-ilmenau.de

[1] Note that we leave out the related fields of electrochemistry, combustion, and research on Belousov-Zhabotinsky reaction-type systems.

including the impact of various physical properties on flow regimes, in a chemical system well documented in a series of experimental and theoretical publications [27–31].

The system is an aqueous solution of methylene-blue–glucose with continuous supply of oxygen through the top air-liquid interface. This oxygen supply causes the production of dense gluconic acid preferentially near the top, which leads to a gravitationally unstable situation. Bees *et al.* [28] have proposed a mathematical model for this reaction and conducted a linear stability analysis [28] of the time-dependent reaction-diffusion state within a quasi-steady-state approximation. The predicted onset time of convection and the associated pattern wavelengths were in agreement with the general trends observed in experiments [27]. Later, Pons *et al.* [29] published a detailed experimental analysis of this system in terms of time of instability onset and its associated spatial scales for different experimental conditions (viscosity, layer depth, pH value).

The importance of boundary conditions for this system was demonstrated in two papers. First, a weakly nonlinear analysis [30] found decreasing wave numbers for a fixed oxygen flux boundary condition at the liquid-air interface, which is seen in the long-term evolution in the experiments. Second, two-dimensional nonlinear simulation [31] showed how different oxygen boundary conditions influence the numerical solution. In the present work, motivated by these former observations, we extend the physical model by including an air layer, since the appropriate oxygen boundary conditions appeared uncertain in the one-phase approach [31].

The work is divided into two parts. First, we extend the stability methods of Ref. [28] by determining an optimal initial perturbation [32]. This method allows us to study the stability of the unsteady but quiescent reaction-diffusion basic state. Considering the basic state as fully unsteady implies solutions for the linearized perturbations that are not purely exponential in time; one speaks of nonmodal stability [33] or non-normal mode [34] referring to the more mathematical approach. Second, we show how the different time scales employed in the problem lead to differences in the convective structure of nonlinear states.

Section II introduces the physical problem based on former experimental works [27,29]. Nondimensional governing equations are summarized in Sec. III. Section IV introduces three sets of parameters which correspond to different reaction rates and/or layer heights [29], namely type I (reference), type II (high reaction rates), and type III (deep fluid layer). Section IV describes the *basic state*. It corresponds to a system with no convective transport, evolving under the action of pure diffusion and chemical reactions. Section VI studies the onset of convection by applying the optimal linear stability method to the chemoconvection system. Thereafter, the onset of convection is again determined but now based on the results of direct numerical simulations (DNS) under optimal and random initial perturbations (Sec. VII). The results of the DNS after onset are discussed in Sec. VIII. The time evolution is divided into two periods. Right after onset (the *onset phase*), the flow pattern is determined by a sudden release of potential energy. These flow structures, which are rather similar for the three parameter sets, are presented in Sec. VIII A. In a second period, the pattern shape and evolution depends on the three parameter sets (types I, II, and III). In Sec. VIII B 1, the flow structure for type I is described as convection cells with continuously growing length scales. Section VIII B 2 addresses types II and III which evolve into a statistically stationary state with an erratically located emission of solutal plumes. Finally, we compare our results to former results from numerical simulations (Sec. VIII C) and experiments (Sec. VIII D). The final Sec. IX presents our conclusions.

II. THE CHEMOCONVECTION SYSTEM

Pons *et al.* [27,29] reported a system where convection was caused by a density difference due to the alkaline oxidation of glucose with methylene blue as catalyst. More precisely, an aqueous solution of glucose GL, sodium hydroxide NaOH, and methylene in two forms (colorless reduced form MBH and colored oxidized form MB^+) is poured into a Petri dish which is then covered by a lid. The Petri dish of total height $H = d + l$ contains a liquid layer of thickness d and an air layer of thickness l (Fig. 1). Initially, this solution is saturated with oxygen O_2 and appears uniformly blue because the colorless form MBH has been oxidized [27] to its colored form MB^+ through the chemical reaction

$$2\mathrm{MBH} + \mathrm{O}_2 \xrightarrow{k_1} 2\mathrm{MB}^+ + 2\mathrm{OH}^-, \tag{1}$$

characterized by a fast reaction rate k_1. A second chemical reaction is also taking place: It is the reduction [27]

$$\mathrm{GL} + \mathrm{MB}^+ + \mathrm{OH}^- \xrightarrow{k_{\mathrm{obs}}} \mathrm{MBH} + \mathrm{GLA}, \tag{2}$$

with a much slower reaction rate k_{obs}, which produces gluconic acid GLA by the consumption of glucose GL. Since the reaction rate of oxidation (1) is much larger than that of reduction (2), it is the oxygen supply that drives the production of GLA through the production of the two components MB^+ and OH^- that mainly act as catalysts.

The oxygen initially present in the bulk is gradually consumed by oxidation (1). Thereafter, the oxygen is only supplied through the air-liquid interface and then diffuses into the bulk. At this stage, the oxygen consumed by oxidation (1) can be only partially compensated by its diffusion from the air layer into the liquid layer and, obviously enough, this effect increases as one gets away from the surface. By consequence, the production of MB^+ by oxidation decreases with growing distance from the interface. Away from the surface, the product MB^+ is hence consumed by reaction (2)

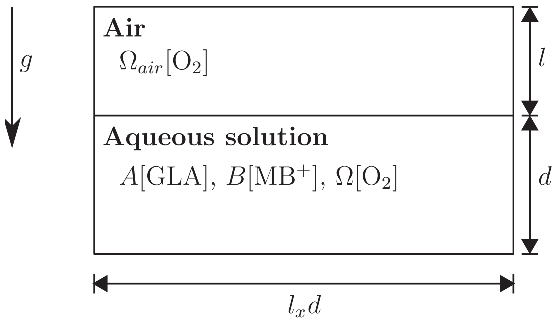

FIG. 1. Sketch of the chemoconvection experiment inside a covered Petri dish.

TABLE I. Definition of material properties and numerical parameters fixed for all three sets of parameters. Most of these values are given in Table 2 of Ref. [29]. The diffusivity of oxygen in air is estimated from Ref. [35] and the initial oxygen concentration in the liquid is estimated from Ref. [27]. We assume the initial molar concentration of oxygen in the air layer to be equal to a common value 8.65×10^{-3}mol/l. This initial molar concentration is deduced from the molar fraction of oxygen in air (= 0.209) given in Table 12.1 from textbook [36], the molar mass of air 28.97g/mol and air density 1.20g/l. From the initial concentration of oxygen in the air and liquid, we deduce the Henry constant $c_H = 33.28$. For acceleration due to gravity we adopted the value of Pons *et al.* [31] $g = 10\,\mathrm{m/s^2}$.

Name	Description	Value	Unit
D_M	Diffusivity of MBH and MB^+	4×10^{-10}	$m^2\ s^{-1}$
D_A	Diffusivity of GLA	6.7×10^{-10}	$m^2\ s^{-1}$
D_Ω	Diffusivity of oxygen O_2 in liquid	2.11×10^{-9}	$m^2\ s^{-1}$
$D_{\Omega-\mathrm{air}}$	Diffusivity of oxygen O_2 in air	2.1×10^{-5}	$m^2\ s^{-1}$
$\Delta\rho$	Excess solution density per mole of GLA	44	kg $m^{-3}(\mathrm{mol/l})^{-1}$
W_0	Initial concentration of MBH + MB^+	4.6×10^{-5}	mol/l
Ω_S	Initial concentration of O_2 in the liquid	2.6×10^{-4}	mol/l
H	Height of the Petri dish	2.7×10^{-2}	m
c_H	Henry constant	33.28	(mol/l)/(mol/l)
$\delta_\Omega = \frac{D_\Omega}{D_M}$	Diffusion ratio of O_2 in liquid to MB^+	5.28	—
$\delta_A = \frac{D_A}{D_M}$	Diffusion ratio of GLA to MB^+	1.68	—
$\delta_{\mathrm{air}} = \frac{D_{\Omega-\mathrm{air}}}{D_M}$	Diffusion ratio of O_2 in air to MB^+	5.25×10^4	—

and not renewed through reaction (1). Consequently, the solution slowly becomes colorless as the concentration of MB^+ decreases while it is replaced by the colorless form MBH and reaction (2) slows down because of the lack of MB^+, which causes a diminished production of gluconic acid from glucose. By contrast, oxygen is still available near the interface, and both reactions are active: The solution keeps its blue color and the production of gluconic acid GLA is still going on. As a result, the gluconic acid gradually accumulates on the top layer. This fluid rich in acid is slightly denser than fluid with pure glucose [the excess density of GLA with respect to GL per unit mole $\Delta\rho = \rho_{\mathrm{GLA}} - \rho_{\mathrm{GL}}$ is equal to 44 $(\mathrm{kg/m^3})/(\mathrm{mol/l})$] [28], i.e., the local density increases near the surface. Finally, this accumulation of GLA produces a difference in density able to generate a gravitational instability initiating convection in the fluid.

In these experiments [29], Marangoni instability was avoided and the possibility of classical Rayleigh-Bénard instability was excluded. The main results obtained in these experiments are the times necessary for convection onset and the corresponding pattern wavelength. Pons *et al.* reported these data for several experimental conditions: NaOH concentrations, layer depths, and temperatures were modified as well as viscosity by adding polyethylene oxide PEO.

III. PHYSICAL MODEL

In order to get close to the experimental situation, we consider a dynamical model including two phases: a liquid layer and an air layer completely closed in a Petri dish. This differs from Bees *et al.* [28], where a boundary condition for the oxygen was set. In both layers, the physical quantities are taken to be periodic in the horizontal directions for the sake of computational performance. The periodicity length is $l_x d$ along the x direction and $l_y d$ along the y direction. All material parameters used to describe the physical system are given in Tables I and II.

In the liquid phase, the dynamics are described by the mass-momentum transport equations coupled to the chemical reaction equations introduced by Bees *et al.* [28]. We thus limit the presentation to the essentials. (For more details, the reader is urged to consult Ref. [28].) The fluid motion satisfies the Boussinesq approximation, i.e., density differences are neglected except in the buoyancy term [see Eqs. (3) and (4)]. In a typical experiment, the initial concentrations of GL and OH^- are so large that they can be considered constant over a long period. Moreover, the sum W_0 of the concentrations of MB^+ and MBH remains constant in space and in time if its initial distribution is homogeneous in space and diffusivities of MB^+ and MBH are equal. If these assumptions are satisfied, it is sufficient to consider an equation for the oxidized form methylene blue MB^+. Consequently, in the liquid phase, only the concentrations of gluconic acid GLA, oxidized-form methylene blue MB^+, and dissolved oxygen O_2 are modeled by their advection-reaction-diffusion Eqs. (5)–(7).

In the air phase, the oxygen transport is assumed to be purely diffusive [Eq. (8)]. This is justified by the low Schmidt number in air $\mathrm{Sc}_{\mathrm{air}} \approx 0.5$ and *a posteriori* by a low Reynolds number imposing a small Peclet number $\mathrm{Pe} = \mathrm{ReSc} < 1$. The upper boundary of the air layer is taken to be impermeable which corresponds to the covered Petri dish of experiments in Ref. [29]. Finally, the ratio between the concentration of oxygen in the air and liquid is in equilibrium at the air-liquid interface through Henry's law with constant c_H (see Table I).

In order to put the system in nondimensional form, we adopt the fluid layer height as characteristic length $\tilde{L} = d$. If one excepts this scale, the remaining characteristic units $(\tilde{T}, \tilde{V}, \tilde{P})$ for nondimensionalization are motivated by the work of Bees *et al.* [28]. The time is nondimensionalized with the inverse dimensional reaction rate $\tilde{T} = k_{\mathrm{obs}}^{-1}$ of the slow reaction [Eq. (2)], reflecting the reduction (decolorization) of MB^+. In this unit, the conversion of the GL into GLA takes roughly one dimensionless time unit. The velocity is accordingly scaled by $\tilde{V} = dk_{\mathrm{obs}}$. Pressure is nondimensionalized by $\tilde{P} = \mu k_{\mathrm{obs}}$ where μ stands for the dimensional liquid dynamic viscosity.

TABLE II. Physical properties and numerical parameters that vary with the three experimental parameter sets. Viscosity and reaction rates are modified by temperature and NaOH concentration. The reaction rates are measured at 19 °C in Fig. 14 of Pons *et al.* [27]

Name	Description	Value Type I (exp. 12)	 Type II (exp. 7)	 Type III (exp. 11 ext.)	Unit
$d = \tilde{L}$	Liquid layer height	8×10^{-3}	8×10^{-3}	20×10^{-3}	m
k_1	Fast reaction rate [Eq. (1)]	2675	19826	2000	$(\mathrm{mol/l})^{-1}\ \mathrm{s}^{-1}$
$k_{\mathrm{obs}} = \tilde{T}^{-1}$	Slow reaction rate [Eq. (2)]	0.0036	0.0496	0.0042	s^{-1}
μ	Dynamic viscosity (∼water)	1.05×10^{-3}	1.0×10^{-3}	1.0×10^{-3}	$\mathrm{kg\ m^{-1}\ s^{-1}}$
ν	Kinematic viscosity	1.053×10^{-6}	1.0×10^{-6}	1.0×10^{-6}	$\mathrm{m^2\ s^{-1}}$
$H_\Omega = \sqrt{D_M/k_{\mathrm{obs}}}$	Oxidation layer height	0.33×10^{-3}	0.09×10^{-3}	0.31×10^{-3}	m
$\delta_l = \frac{l}{d} = \frac{H-d}{d}$	Ratio air-liquid height	2.375	2.375	0.35	—
$\kappa = \frac{2k_1\Omega_S}{k_{\mathrm{obs}}}$	Reaction ratio	385	220	248	—
$\lambda = \frac{k_1 W_0}{k_{\mathrm{obs}}}$	Reaction ratio	34.1	19.5	21.9	—
$\delta_d = \frac{d}{H_\Omega}$	Liquid height to oxid. region	24	86.62	64.81	—
$R = \frac{g\Delta\rho W_0 {H_\Omega}^3}{\mu D_M}$	Rayleigh number	1.73	0.04	1.49	—
$\mathrm{Sc} = \frac{\mu}{\rho D_M}$	Schmidt number	2632.5	2500	2500	—
$T_{\mathrm{diff}} = \frac{d^2 k_{\mathrm{obs}}}{D_M}$	Nondim. diffusion time	576	7503	4200	—
$T_{\mathrm{vis}} = \frac{d^2 k_{\mathrm{obs}}}{\nu}$	Nondim. viscous time	0.22	3.0	1.68	
$R\delta_d$	Modified Rayleigh number	41.52	3.46	96.56	—

The concentrations of gluconic acid GLA and the oxidized form of methylene blue MB^+ are nondimensionalized by W_0 the homogeneous total concentration of methylene blue MB^+ plus MBH, a quantity which was fixed for all experiments. Finally, the oxygen concentration in air and water is scaled by its initial concentration Ω_S in water at 19 °C. From now on, $\mathbf{u} = (u_x, u_y, u_z)$ and P denote the nondimensional velocity field and the dynamical pressure, respectively. Similarly, the nondimensional concentrations of gluconic acid, the oxidized form of methylene blue, the oxygen in aqueous solution and the oxygen in air are denoted by A, B, Ω, and Ω_{air}, respectively (Fig. 1). All nondimensional quantities that appear in the dimensionless governing equations or conditions are summarized in Tables I and II.

The full nondimensional equations in the liquid domain $0 < x < l_x$, $0 < y < l_y$, $0 < z < 1$ read

$$\frac{\delta_d^2}{\mathrm{Sc}}\left[\frac{\partial \mathbf{u}}{\partial t} + (\mathbf{u}\cdot\nabla)\mathbf{u}\right] = -\nabla P - \delta_d R A \mathbf{e}_z + \nabla^2 \mathbf{u}, \tag{3}$$

$$\nabla \cdot \mathbf{u} = 0, \tag{4}$$

$$\frac{\partial A}{\partial t} = -\nabla \cdot \left(A\mathbf{u} - \frac{\delta_A}{\delta_d^2}\nabla A\right) + B, \tag{5}$$

$$\frac{\partial B}{\partial t} = -\nabla \cdot \left(B\mathbf{u} - \frac{1}{\delta_d^2}\nabla B\right) + \kappa\Omega(1-B) - B, \tag{6}$$

$$\frac{\partial \Omega}{\partial t} = -\nabla \cdot \left(\Omega\mathbf{u} - \frac{\delta_\Omega}{\delta_d^2}\nabla \Omega\right) - \lambda\Omega(1-B), \tag{7}$$

where gravity acts in the negative (vertical) z direction.

In the air layer $0 < x < l_x$, $0 < y < l_y$, $1 < z < 1 + \delta_l$ ($\delta_l = l/d$) the oxygen concentration satisfies the diffusion equation

$$\frac{\partial \Omega^{\mathrm{air}}}{\partial t} = \frac{\delta_{\mathrm{air}}}{\delta_d^2}\Delta\Omega^{\mathrm{air}}. \tag{8}$$

For the velocity field, no-slip conditions are satisfied at the bottom of the Petri dish ($z = 0$),

$$u_z = u_x = u_y = 0 \qquad \text{at } z = 0. \tag{9}$$

The liquid-air interface is assumed to remain flat at $z = 1$ and to be stress free,

$$u_z = \frac{\partial u_x}{\partial z} = \frac{\partial u_y}{\partial z} = 0 \qquad \text{at } z = 1. \tag{10}$$

The concentration fields A, B verify a zero flux condition at the bottom of the Petri dish and at the liquid-air interface

$$\frac{\partial A}{\partial z} = \frac{\partial B}{\partial z} = 0 \qquad \text{at } z = 0,1. \tag{11}$$

An identical condition is imposed to the oxygen concentrations Ω (respectively, Ω^{air}) at the bottom (respectively, at the top) of the covered Petri dish,

$$\frac{\partial \Omega}{\partial z} = 0 \qquad \text{at } z = 0, \tag{12}$$

$$\frac{\partial \Omega^{\mathrm{air}}}{\partial z} = 0 \qquad \text{at } z = 1 + \delta_l. \tag{13}$$

Finally, at the liquid-air interface $z = 1$, oxygen concentrations Ω and Ω^{air} are related by the Henry law as follows:

$$\Omega(z = 1) = \Omega^{\mathrm{air}}(z = 1)/c_H \qquad \text{at } z = 1, \tag{14}$$

and by the conservation of mass fluxes

$$\frac{\partial \Omega}{\partial z} = \frac{\delta_{\mathrm{air}}}{\delta_\Omega}\frac{\partial \Omega^{\mathrm{air}}}{\partial z} \qquad \text{at } z = 1. \tag{15}$$

For the horizontal x and y directions, we assume periodicity for all fields, e.g., $u_x(x + l_x, y, z, t) = u_x(x, y, z, t)$ for all (x, y, z).

IV. PARAMETER SETS

Three different sets of material parameters are introduced and simulated. Type I is characterized by modest reaction rates and a liquid height of $d = 8$ mm. This type refers to experiment 12 in Ref. [29] and is simulated in a two-dimensional setting in Pons *et al.* [31]. Type II is characterized by high reaction rates due to increased NaOH concentration and an identical liquid height $d = 8$ mm. It corresponds to experiment 7 in Ref. [29]. Finally, type III is motivated by the change in liquid layer height in experiments [29]. The largest layer in Ref. [29] was 11.7 mm (experiment 11). However, we set the height to $d = 20$ mm to see a larger effect, while keeping the reaction rate modest in line with experiments [29]. The material properties for these three different types are given in Tables I and II. The parameters related to the experiments (3)–(11) of Pons *et al.* [29] are gathered from Refs. [27] and [28], parameters for experiment 12 are taken from Table 2 in Ref. [29]. In Table II, the associated parameters are provided. The dimensionless viscous time scale T_{vis} and dimensionless diffusive time scale T_{diff},

$$\begin{aligned} T_{\mathrm{vis}} &= \frac{d^2}{\nu \tilde{T}} = \frac{d^2 k_{\mathrm{obs}}}{\nu} = \delta_d^2/\mathrm{Sc}, \\ T_{\mathrm{diff}} &= \frac{d^2}{D_M \tilde{T}} = \frac{d^2 k_{\mathrm{obs}}}{D_M} = \delta_d^2, \end{aligned} \tag{16}$$

are measured in the intrinsic reaction time $\tilde{T}$ units.

V. BASIC SOLUTION

Let us study the stability of the quiescent *basic state* ($\mathbf{u}_0 = 0$) to the onset of convection. This pure reaction-diffusion state $[A_0(z,t),\ B_0(z,t),\ \Omega_0(z,t),\ \Omega_0^{\mathrm{air}}(z,t),\ P_0(z,t)]$ is unsteady and heterogeneous only along the vertical coordinate z. It solves Eqs. (3)–(15) and starts with the initial conditions

$$\begin{aligned} &A_0(z,t=0) = 0,\ \ B_0(z,t=0) = 1,\ \ \Omega_0(z,t=0) = 1, \\ &\Omega_0^{\mathrm{air}}(z,t=0) = c_H. \end{aligned} \tag{17}$$

[The reduced governing equations are shown in Appendix A.] The chemical reactions depend on the initial concentration of dissolved oxygen and on the oxygen diffusion through the liquid-air interface. In the first stage, vertical gradients in the oxygen distribution (oxygen concentration is higher at the top) barely impact the production of B which stays at its maximum value $B = 1$. When the initial amount of oxygen is consumed, the production of B is impacted by the increased oxygen concentration at the top and an unstable A stratification is increasingly formed. The time range when this occurs can be estimated. Assuming that $B = 1$ until all initial oxygen has been exhausted, and observing that 1 mol of oxygen produces 2 mol of oxidized methylene blue B through reaction 1, it takes approximately $T_O = 2\Omega_s/W_0 = \kappa/\lambda = 11.3$ time units to consume all the initial oxygen which in turn leads to a spatial gradient.

Figure 2 displays the concentration profiles of gluconic acid for the basic state at three different times around T_O (increasing order): the experimental onset time, the onset time provided by our DNS results in Sec. VII, and a time in between. The oxygen supply from the top and its conversion into gluconic acid A is readily observed in these profiles. For all three types, a first noticeably unstable stratification is observed at the experimental onset time. The inflection point in the concentration $A_0(z,t)$ profile is located at lower z for type I than type II or III, meaning a deeper penetration of A. This change with parameter sets could be attributed to the characteristic dimensionless diffusion time T_{diff}, since it is smaller for type I than for type II or III (see Table II).

VI. OPTIMAL LINEAR PROCEDURE: CONVECTION ONSET DETERMINATION

A. Optimal linear perturbation: Method

To predict the onset time and corresponding length scales of the convection pattern, an instability analysis of the basic state $[A_0(z,t),\ B_0(z,t),\ \Omega_0(z,t),\ \Omega_0^{\mathrm{air}}(z,t),\ P_0(z,t)]$ is performed.

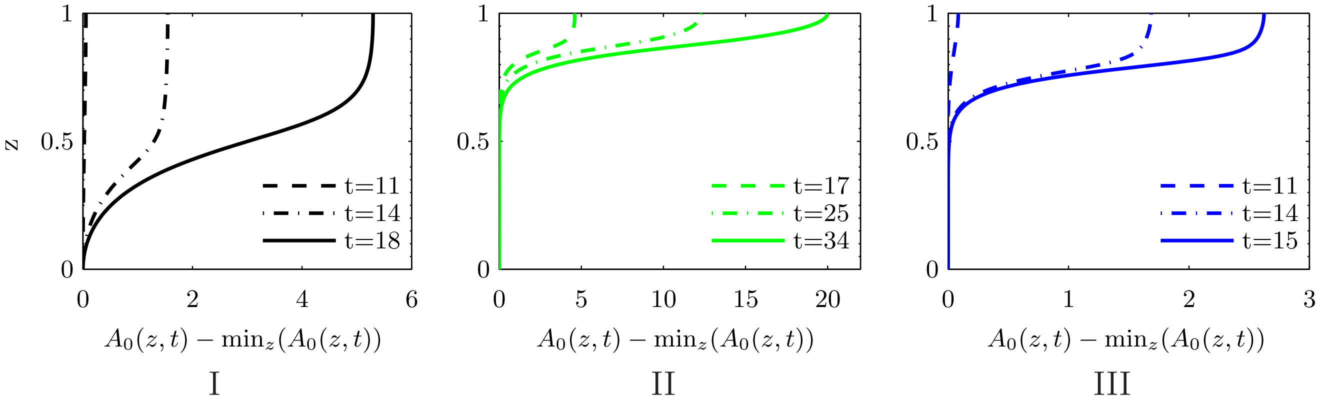

FIG. 2. (Color online) Basic state profiles of gluconic acid A_0 for types I, II, and III at three different times: experimental onset time, which is the earliest time (for type III, we used the value of type I because there is no corresponding experimental data), shortly before the onset provided by the DNS (the largest time) and at time in between. Please observe that the axis numbering changes between the types.

We adopt a method similar to the one used in Ref. [37] which is naturally adapted to unsteady basic states. By means of this method we extend former work [28] in which a standard frozen-time analysis was performed. More precisely, the pattern formation process is studied using a linear stability analysis of the unsteady basic flow: Initial conditions are modeled as a sum of the basic state (at initial time $t = 0$) and an arbitrary perturbation (denoted with subscript p),

$$\mathbf{u} = \mathbf{u}_p(x,y,z,t),\ P = P_0(z,t) + p_p(x,y,z,t), \tag{18}$$

$$A = A_0(z,t) + A_p(x,y,z,t),\ B = B_0(z,t) + B_p(x,y,z,t), \tag{19}$$

$$\Omega = \Omega_0(z,t) + \Omega_p(x,y,z,t),\ \Omega^{\text{air}} = \Omega_0^{\text{air}}(z,t) + \Omega_p^{\text{air}}(x,y,z,t). \tag{20}$$

When perturbations are assumed to be of small amplitude, they satisfy a linear system with no preferential direction in the x-y plane. Without loss of generality, Fourier modes with a wave number α in the x direction and no y dependence can be considered, i.e.,

$$(\mathbf{u}_p, A_p, B_p, \Omega_p, \Omega_p^{\text{air}}, p_p) = \mathbf{q}(z,t)e^{i\alpha x}, \tag{21}$$

where $\mathbf{q}$ is a vector of vertical perturbation profiles

$$\mathbf{q}(z,t) = (\hat{u}, \hat{w}, \hat{A}, \hat{B}, \hat{\Omega}, \hat{\Omega}^{\text{air}}, \hat{p}). \tag{22}$$

Since the basic flow is unsteady, it is not possible to perform a classical normal mode analysis in which mode $\mathbf{q}$ is purely exponential in time. A non-normal approach [33,38], however, can still be used since it handles unsteady basic flows. This approach defines an objective scalar function $E_\beta(\mathbf{q})$ for a perturbation $\mathbf{q}$ (the subscript β is introduced to allow several possible objective functions). The scalar $E_\beta(\mathbf{q})$, which measures the perturbation amplitude, should be properly chosen to emphasize a property related to the instability mechanism. Selecting different functions $E_\beta(\mathbf{q})$ enables one to discuss different possible sources of instability. In the present paper, the objective function is assumed to be a quadratic form

$$E_\beta[\mathbf{q}(t)] = \sum_{j=1}^{6} C_j^\beta \int_0^1 q_j(z,t) q_j^*(z,t)dz, \quad C_j^\beta \in \{1,0\}, \tag{23}$$

where C_j^β are free constants and star * means the complex conjugate. Thereafter, this approach identifies, for any given time $t = T$, the initial disturbance $\mathbf{q}_{\text{opt}}(t = 0)$ which maximizes at time $t = T$, the measure $E_\beta(\mathbf{q}(t = T))$ among the set of possible initial perturbations $\mathbf{q}(t = 0)$ normalized such that $E_\beta(\mathbf{q}(t = 0)) = 1$. The gain for this optimal initial perturbation

$$G_\beta(t = T, \alpha) = \frac{E_\beta[\mathbf{q}_{\text{opt}}(t = T, \alpha)]}{E_\beta[\mathbf{q}_{\text{opt}}(t = 0, \alpha)]} = E_\beta[\mathbf{q}_{\text{opt}}(t = T, \alpha)] \tag{24}$$

then can be computed. The flow is considered unstable at time T if the gain $G_\beta(t = T, \alpha)$ is above a threshold value G^{tresh}. In the result section (Sec. VI B), we assume $G^{\text{tresh}} = 10$.

The role of a specific field (concentration, velocity) for instability is analyzed by choosing the function E_β. We employ four different kinds, namely

$$E_k(\mathbf{q}) = \int [\hat{u}(z,t)\hat{u}^*(z,t) + \hat{w}(z,t)\hat{w}^*(z,t)]dz, \tag{25}$$

$$E_\Omega(\mathbf{q}) = \int \hat{\Omega}\hat{\Omega}^* dz,\ E_A(\mathbf{q}) = \int \hat{A}\hat{A}^* dz, \tag{26}$$

$$E_B(\mathbf{q}) = \int \hat{B}\hat{B}^* dz, \tag{27}$$

to examine velocity perturbations, concentration perturbations in oxygen, gluconic acid, or methylene blue, respectively. The quantity under consideration is exclusively initialized with a perturbation, the others are zeroed. The onset time and characteristic length scale of the instability are identified by a parametric study, i.e., changing T and α and calculating the respective gain $G_\beta(T, \alpha)$.

In order to get the optimal perturbation for a given wave number α, objective function E_β, and time T, the problem is mathematically restated as a variational problem [33,38]. The details of this mathematical procedure are given in Appendix B.

B. Optimal linear perturbation: Results

For the three experimental parameter sets, the onset times and associated length scales are analyzed by considering the linear optimal perturbation for different objective functions: $E_k(\mathbf{q})$, $E_\Omega(\mathbf{q})$, $E_A(\mathbf{q})$, and $E_B(\mathbf{q})$. In Fig. 3, the decadic logarithm $\log_{10} G_\beta(T, \alpha)$ of the optimal amplification gain is displayed as a function of wave number α and time T. The range of both variables is scanned beginning at 0.1 in intervals of 0.1. From these data sets, the onset times and length scales at convection onset can be predicted. This is done as follows: The critical time T_c is the smallest time T for which the gain is larger than the threshold G^{tresh} for at least one wave number denoted by α_c,

$$(T_c, \alpha_c) = \min_T \{(T, \alpha) : (G_\beta(T, \alpha)) > G^{\text{tresh}})\}. \tag{28}$$

Such values are presented for the three experimental types and the four objective functions in Table III.

TABLE III. Onset times and critical wave numbers for the three experimental sets I, II, and III. T_c and α_c are calculated by the Eq. (28) using four different objective functions and $G^{\text{tresh}} = 10$. The simulated onset time T_{onset} (last row) is calculated [cf. Eq. (29)] from the large box simulations. The corresponding wave number α_{onset} is equal to $k_{\text{avg}}^B(T_{\text{onset}})$ the averaged wave number [see Eq. (D6)] from the Fourier spectrum of $\bar{B}(x, y, t = T_{\text{onset}})$.

	Type I		Type II		Type III	
	T_c	α_c	T_c	α_c	T_c	α_c
E_A	12.5	2.8	14.8	3.8	11.1	3.9
E_Ω	14.2	2.8	18.5	4.1	12.1	3.5
E_B	14.8	3.2	20.7	4.5	12.9	3.8
E_k	18.2	3.6	34.2	4.5	15.4	4.1
	T_{onset}	α_{onset}	T_{onset}	α_{onset}	T_{onset}	α_{onset}
DNS	18.4	3.7	34.8	4.5	15.8	4.1

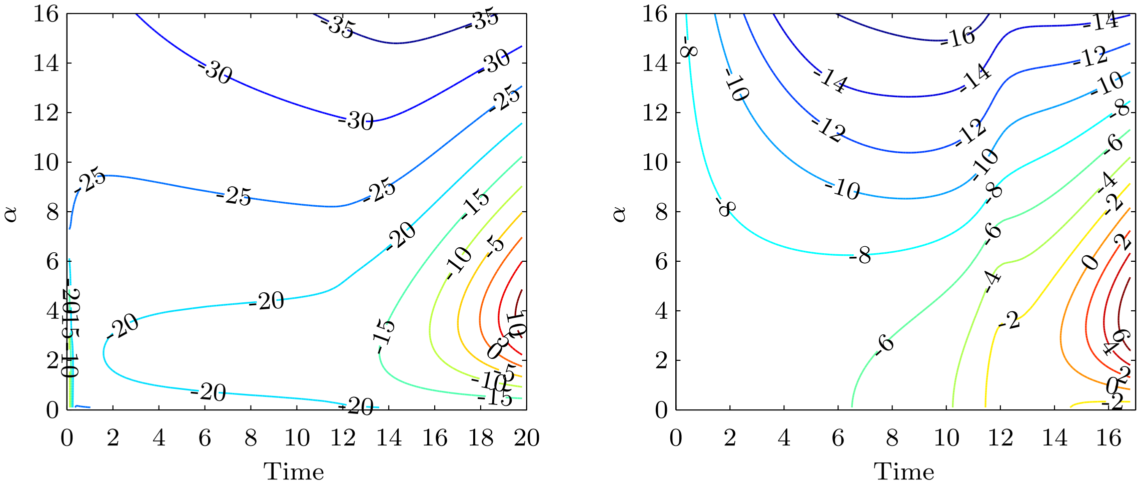

(a)$\log_{10}(G_k)$ (b)$\log_{10}$ (G_B)

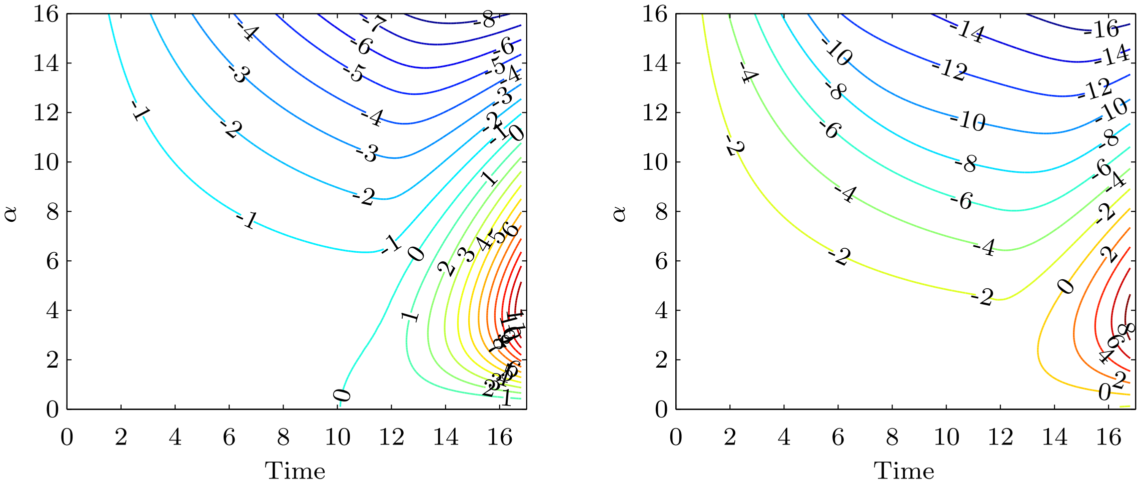

(c)$\log_{10}$ (G_A) (d)$\log_{10}$ (G_Ω)

FIG. 3. (Color online) Logarithm of the gain $G_\beta(t = T,\alpha)$ for different objective functions as a function of the wave number α and the time T. Physical parameter of type I are used.

The onset times [see Fig. 3(c) and Table III] are lowest for E_A, i.e., for concentration perturbations. This is in line with the frozen time analysis [28], since the A perturbations dominate these eigenfunctions (see Fig. 9 in Bees *et al.* [28]). Moreover, this former eigenvalue analysis revealed that the system is most unstable to modes with a wave number near zero. This branch of unstable modes is also observed in Fig. 3(c) where the neutral curve [contour level $\log_{10}(E_A(T,\alpha)) = 0$] approaches the time axis. This trend might be preserved also for values $\alpha < 0.1$ (not calculated here), since an acid perturbation with no spatial variation ($\alpha = 0$) solves the perturbation equations, which yields a gain $G_A(t) = 1$ for all $t \geqslant 0$. However, small-wave-number modes are amplified only very weakly and they demand an experimental device with a large aspect ratio, thus they are physically less relevant.

The type III system gives the earliest onset times when comparing perturbations from one class. It is followed by type I. The onset time is therefore negatively correlated with the modified Rayleigh number $R\delta_d$, i.e., the prefactor of the buoyancy term in Eq. (3), as one might expect.

VII. THREE-DIMENSIONAL NONLINEAR SIMULATIONS: CONVECTION ONSET DETERMINATION

The onset time of convection is now analyzed using three-dimensional (3D) direct numerical simulations starting with random (Sec. VII A) or optimal velocity (Sec. VII B) perturbations. In both cases, initial concentration perturbations are set to zero. This choice corresponds to an initially well-mixed state, which could be approached in experiments. In contrast, stirring or even the basic preparation of a sample unavoidably introduces velocity perturbations to the system. However, we briefly discuss simulations with additional pertubations in the acid field in Sec. VII C.

The full nonlinear model is solved with a pseudospectral method formerly used in Refs. [39,40]. The spatial flow domain is discretized with $N_x \times N_y$ Fourier modes in the horizontal directions and N_z Chebychev polynomials in the vertical direction. Appendix C provides further details of the numerical procedure.

A. Random velocity perturbation

We analyzed the three experimental types. First, a set of type I simulations corresponding to experiment 12 in Ref. [29] is considered. The initial perturbations are built as follows. A random velocity field is first generated: At each grid point, the vertical velocity $u_z(x,y,z)$ and vertical vorticity $\omega_z(x,y,z)$ are set independently and equally distributed in the interval between zero and unity. This field is thereafter multiplied by a factor to produce a random field such that the mean energy $\frac{1}{2}\langle \mathbf{u}^2\rangle_{xyz}(t=0)$ takes one of the values $10^{-6}, 10^{-3}, 10^{0}, 10^{+3}, 10^{+6}$. This amplitude variation is performed with one unique random field which is scaled, respectively. (However, simulations with different random velocity field show only minor variation.) For these simulations, we take $l_x = l_y = 10$ and $N_x = N_y = 512$.

For all amplitudes [Fig. 4(a)], the qualitative temporal evolution of velocity perturbations is similar. First, the initial kinetic energy is dissipated until a minimum is reached proportional to the initial perturbation amplitude. Thereafter, a growth is observed leading to convection. In order to determine the onset time, we consider the observed methylene pattern via the vertical average $\bar{B}(x,y,t)$ (cf. Appendix D for the definition and notation). This is reminiscent of the experiments [29], since $\bar{B}(x,y,t)$ is a direct measure of the light absorption. Using this DNS data, the onset time is defined as the time when the variance $\sigma_B^2(t)$ [see Eq. (D8) in Appendix D] in the observed methylene-blue pattern $\bar{B}(x,y,t)$ exceeds a critical value σ_c, i.e.,

$$T_{\text{onset}} = \min\{t : \sigma_B(t) > \sigma_c\}. \tag{29}$$

This critical value σ_c is not explicitly given in Refs. [29,31]. However, given that the experimental device [29] has a resolution of 256 gray values between zero and 1 for $\bar{B}(x,y)$, a standard deviation of $\sigma_c = 1/256$ seems an appropriate threshold for detection of convection. For the random velocity perturbations, T_{onset} can be a fitted [Fig. 4(b)] by

$$T_{\text{onset}}^{\text{random}} = 18.51 - 0.1742 \log_{10}\left(\tfrac{1}{2}\langle \mathbf{u}^2\rangle_{xyz}(t=0)\right).$$

The logarithmic dependence on the amplitude is readily explained by assuming an exponential growth of perturbation.

The onset time T_{onset} for type I and $\frac{1}{2}\langle \mathbf{u}^2\rangle_{xyz}(t=0) = 1$ is recorded together with the linear prediction in Table III. (There we used the simulated data from a larger domain $l_x = l_y = 20$ with $N_x = N_y = 1024$ and $N_z = 128$; onset time is almost identical to $l_x = l_y = 10$.) A reasonable agreement with the optimal-linear prediction for velocity perturbation E_k is observed. The critical wave number is also computed. It is obtained as in Ref. [29], by a Fourier analysis of the methylene-blue distribution $\bar{B}(x,y)$ [similarly, the acid distribution $\bar{A}(x,y)$ could be considered] providing a power spectrum $H_2^B(k,t = T_{\text{onset}})$. From the power spectrum $H_2^B(k,t = T_{\text{onset}})$ at onset, the wave number is identified with the weighted average $\alpha_{\text{onset}} \equiv k_{\text{avg}}^B(T_{\text{onset}})$ according to Eq. (D6). At onset this wave number compares well to the one from the optimal linear analysis with objective function E_k for perturbation velocity (see Table III).

The chemoconvection results were also analyzed for types II (experiment 7) and III (experiment 13). These simulations were also initiated by a random velocity field with $\frac{1}{2}\langle \mathbf{u}^2\rangle_{xyz}(t=0) = 1$ and computed in a large domain ($l_x = l_y = 20$ for type II or $l_x = l_y = 8$ for type III with $N_x = N_y = 1024$ and $N_z = 128$). Again, the onset times T_{onset} and wave number $k_{\text{avg}}^B(T_{\text{onset}})$ at onset compare well to the one from the optimal linear prediction based on E_k (see Table III).

B. Optimal velocity perturbations

Due to horizontal translational invariance of the linearized equations, the optimal growth analysis can only provide the

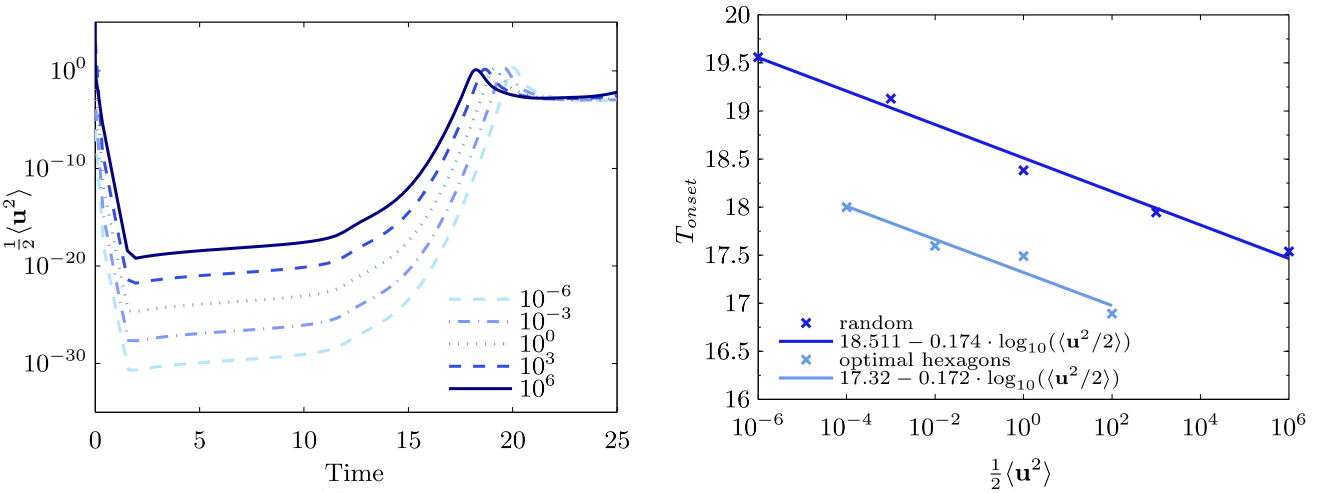

(a) (b)

FIG. 4. (Color online) Three-dimensional simulations of type I. (a) Quantity $\frac{1}{2}\langle \mathbf{u}^2\rangle_{xyz}(t)$ for random initialized velocity field with different initial amplitudes. (b) Onset times computed using criterion [Eq. (29)] for random initialized velocity field and for an optimal initial condition (hexagons) with a wave number $\alpha_{\text{opt}} = 3.6$.

vertical perturbation structure and wavelength. The horizontal structure of the pattern is not determined in this way. In order to study optimal profiles, we take it to be spatially periodic as in stationary convection problems, i.e., with a hexagonal, square, or linear (roll) pattern. Type I (experiment 12 in Ref. [29]) is analyzed in this way using a series of simulations. The z profile and critical wave number α_c are those of the optimal velocity perturbations, i.e., obtained by the objective function E_k.

For hexagons, the vertical velocity is initialized with the Christopherson solution [4]

$$u_z = \hat{w}(z)\left[\cos\left(\alpha_c\left(\frac{\sqrt{3}}{2}y - \frac{1}{2}x\right)\right) + \cos(\alpha_c x) + \cos\left(\alpha_c\left(\frac{\sqrt{3}}{2}x + \frac{1}{2}y\right)\right)\right], \quad (30)$$

while the horizontal velocity components result from the incompressibility condition and imposing the vertical vorticity to be zero. For a square pattern the vertical velocity is

$$u_z = \hat{w}(z)[\cos(\alpha_c y) + \cos(\alpha_c x)], \quad (31)$$

and for the roll pattern it is

$$u_z = \hat{w}(z)[\cos(\alpha_c x)]. \quad (32)$$

The onset time computed using this optimal perturbation leads to an earlier onset of convection. The three patterns yield nearly the same onset time. The derived onset times for an initial amplitude of $\frac{1}{2}\langle \mathbf{u}^2\rangle_{xyz}(t=0) = 1$ and $\alpha_{\text{opt}} = 3.6$ are, for example, 17.50 (hexagons), 17.53 (squares), and 17.54 (rolls). Furthermore, the optimal patterns display an analogous logarithmic dependency on the initial amplitudes as the random initial perturbations [Fig. 4(b)].

C. Random perturbations of acid concentration and velocity

The impact of an initial perturbation in both the acid-concentration field and the velocity field is studied now. Velocity is initialized as described in Sec. VII A,with a unity amplitude $\frac{1}{2}\langle \mathbf{u}^2\rangle_{xyz}(t=0) = 1$ for all runs. The acid perturbation is varied, its concentration is initialized with numbers equally distributed between zero and 1. Then we adjust the squared mean value $\langle (A(x,y,z,t=0))^2\rangle_{xyz} = 0.01,1,100$ by multiplying with a common prefactor. Thereby, three simulations are performed with independent random initial conditions.

As expected, the onset time decreases with growing perturbation strength, i.e., $T_{\text{onset}} = 14.78(0.01), 13.18(1), 11.58(100)$. These times again compare reasonably with the time $T_c = 12.5$ predicted by the linear analysis, cf. Table III. Except for the onset time, the behavior of simulations with perturbations of acid concentration show no distinct features compared to runs where only the velocity is perturbed.

VIII. THREE-DIMENSIONAL NONLINEAR SIMULATIONS: RESULTS

The system evolution for the three different simulations (types I, II, and III[2]) is presented in Fig. 5 where the chemical species volume average is shown until $t = 200$. The onset time by the criterion defined in Eq. (29) is pinpointed by red crosses. Before onset, oxygen concentration and methylene-blue concentration are clearly decreasing for the three simulations. After convection onset, the time range can be subdivided into two characteristic phases. Just after onset (called the *onset phase*), kinks or minor oscillations appear in $\langle B\rangle_{xyz}$. Thereafter, the system continuously develops into a *quasisteady state* for $\langle B\rangle_{xyz}$ and $\langle\Omega\rangle_{xyz}$, which differs for the three cases. The Reynolds number based on the rms velocity,

$$\text{Re} = \frac{\sqrt{\langle \mathbf{u}\cdot\mathbf{u}\rangle_{xyz}}\tilde{V}d}{\nu} = T_{\text{vis}}\sqrt{\langle \mathbf{u}\cdot\mathbf{u}\rangle_{xyz}}, \quad (33)$$

is almost constant and below unity in this second phase [Fig. 6(a)] though inertial effects are larger for types II and

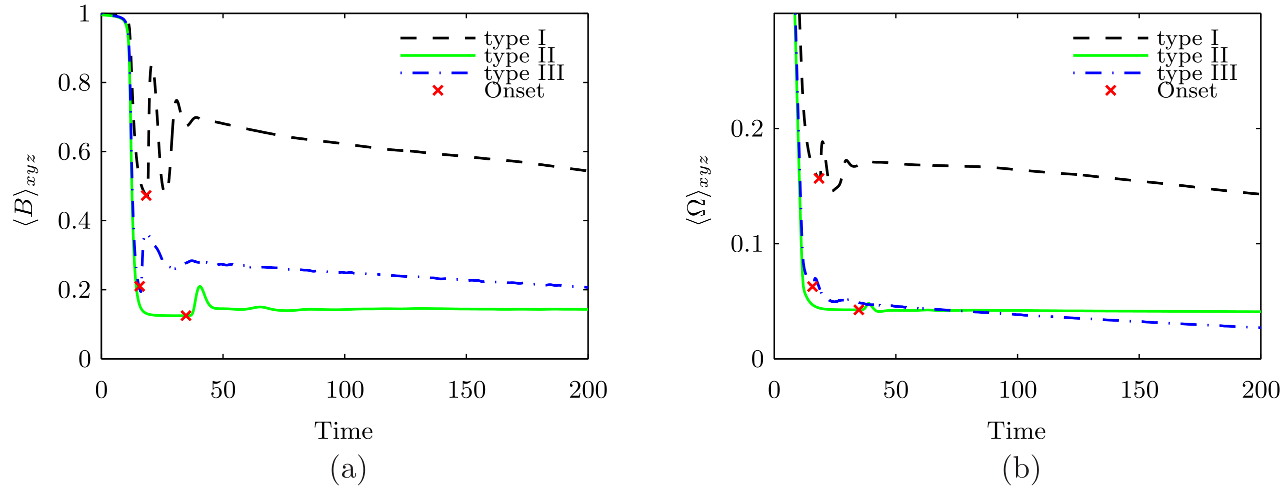

(a) (b)

FIG. 5. (Color online) Three-dimensional simulations of types I, II, and III. (a) Volume average of methylene blue B; (b) volume average of oxygen Ω dissolved in the liquid. The onset times for the three simulations are marked by crosses ($T^{\text{I}}_{\text{onset}} = 18.44$, $T^{\text{II}}_{\text{onset}} = 34.8$, $T^{\text{III}}_{\text{onset}} = 15.8$).

---

[2] The results presented in Sec. VIII are based on simulations in a large square domain of size 16 × 16 cm, which is introduced at the end of Sec. VII A.

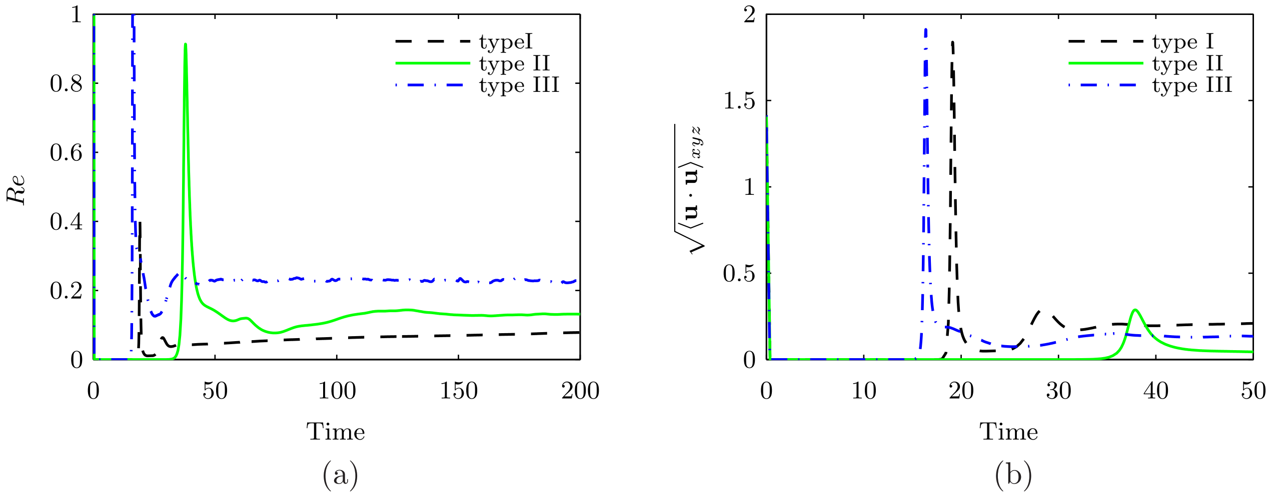

FIG. 6. (Color online) Three-dimensional simulations of types I, II, and III. (a) Reynolds number; (b) rms velocity.

III compared to type I [Fig. 6(a)]. Since the Peclet number Pe = ReSc is of order Pe $\sim 10^1$–10^2 for all three cases, the solute transport is dominated by advection.

A. Onset phase

Before convection onset, diffusion of oxygen through the liquid-air interface leads to increasingly unstable density stratifications. This is the process which is active for the basic state (see the gluconic acid profiles in Fig. 2). For a more general, horizontally nonuniform flow, this aspect may be quantified by the growth of the quantity

$$e_{\text{pot}} = R\delta_d\big(\langle zA\rangle_{xyz} - \tfrac{1}{2}\langle A\rangle_{xyz}\big), \tag{34}$$

which is related to the total potential energy defined relative to a homogeneous reference state. Potential energy e_{pot} grows in time when all oxygen is exhausted around $t = 11$ [see Fig. 7(a)] with a fairly constant slope. This slope is governed by diffusion of oxygen into the layer, the two chemical reactions leading to denser product, i.e., the gluconic acid A, as well as the diffusive spreading of A which lowers the potential energy density.

This growth stops at convection onset. The increasing rms velocity [see Fig. 6(b)] at the same time indicates that it corresponds to the downward transport of A by convection. Indeed, in Fig. 8(a), a vertical cut at $y = 15$ shows the dense acid layer at onset ($t = 35$), its detachment from the upper interface ($t = 38$), and its impingement on the bottom ($t = 40$), leading to mushroom shapes. Figure 8(b) provides a three-dimensional picture at $t = 38$ with an isosurface of the acid field. The comparable amount of potential energy at convection onset leads, for types I and III, to a comparable maximum velocity amplitude [see sharp peak in Fig. 6(b)]. It is smaller for type II.

This onset phase lasts for $18.4 \leqslant t \leqslant 40$ (type I), $34.8 \leqslant t \leqslant 100$ (type II), and $15.8 \leqslant t \leqslant 40$ (type III). During the beginning of the onset phase, the flow pattern is quite similar in the three types: Polygonal cells emerge with downflow at the

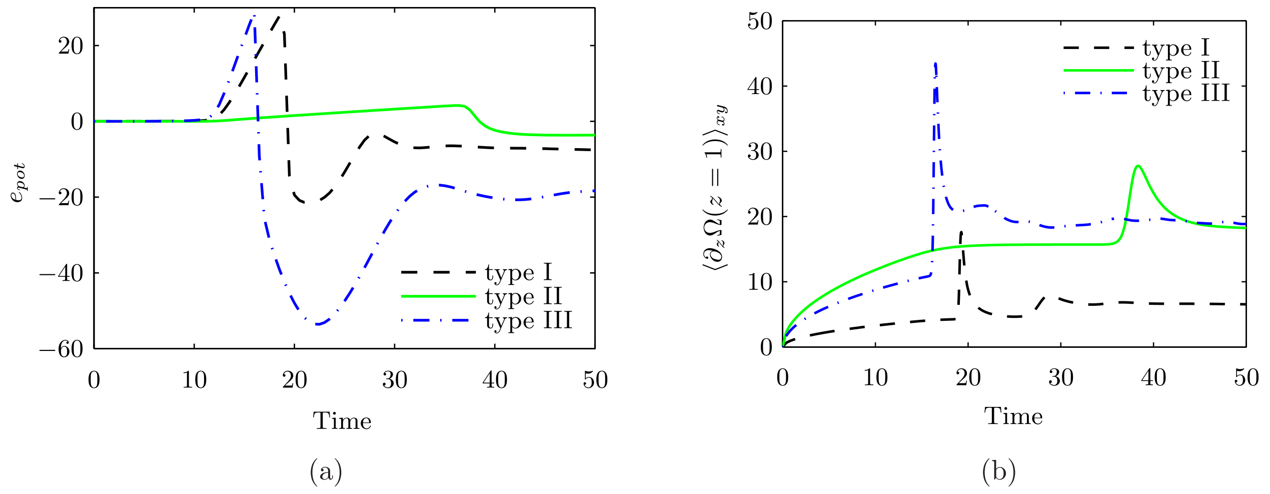

FIG. 7. (Color online) Three-dimensional simulations of types I, II, and III. (a) Potential energy ($e_{\text{pot}} = R\delta_d(\langle zA\rangle_{xyz} - \frac{1}{2}\langle A\rangle_{xyz}$); (b) oxygen gradient at the interface.

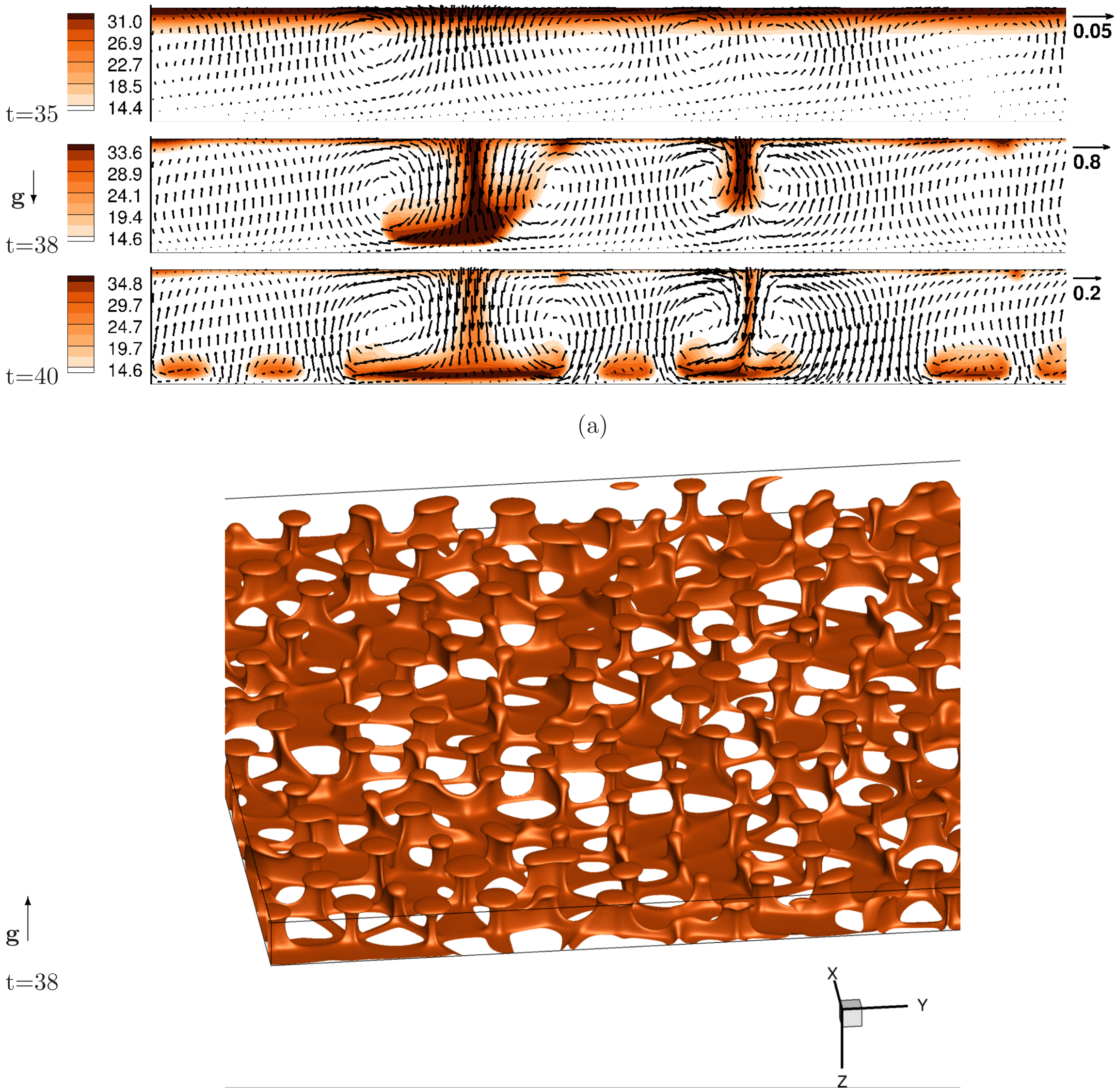

(a)

(b)

FIG. 8. (Color online) Onset phase in 3D simulations for type II ($34.8 \leqslant t \leqslant 100$). (a) Plots of $A(x,y=15,z,t)$ at constant $y=15$ and a subrange of $x \in [0,8]$ at different times. The arrows represent the velocity field tangentially to the cutting plane plane $y=15$. (b) Isosurface at $A(x,y,z,t) = 31.2 = (\max_{[xyz]}(A) - \min_{[xyz]}(A))0.8 + \min_{[xyz]}(A)$ for time $t=38$. Note that gravity is directed downwards in (a) and upwards in (b).

edges. This is illustrated in the first row of Fig. 9 (type II) and Fig. 10 (type I) for the vertically averaged acid concentration $\langle A(x,y,z,t)\rangle_z$. As the initial pattern wave number (Table III) is around four for all three cases, the emerging roll cells have a horizontal size between one and two layer heights (Fig. 8). For types II and III, one observes downwelling plumes (dotted shapes) together with the downflowing "curtains" (Fig. 9) later during the onset phase. Type I keeps the polygonal pattern (Fig. 10).

The change of rms velocity is also associated with the rapid raise of the oxygen gradient at the interface [Fig. 7(b)]. Note that the amplitude of the velocity field in Fig. 6(b) and oxygen gradients in Fig. 7(b) decrease with time but the onset pattern is preserved.

B. Second-phase regime

The dimensionless viscous T_{vis} and diffusive T_{diff} time scales [see Eq. (16) and Table II] indicate that type I differs from types II and III: Viscous momentum transport occurs faster than the chemical reaction, and for types II and III the chemical reaction is faster. The time evolution indeed differs substantially for type I and the two other types.

1. Second phase for type I: Coarsening regime

After the onset phase, flow structures develop into growing cells as seen from the patterns of Fig. 10 and Fig. 11. The cell coarsening can be seen also in a vertical plane displaying the distribution of acid A together with the tangential velocity

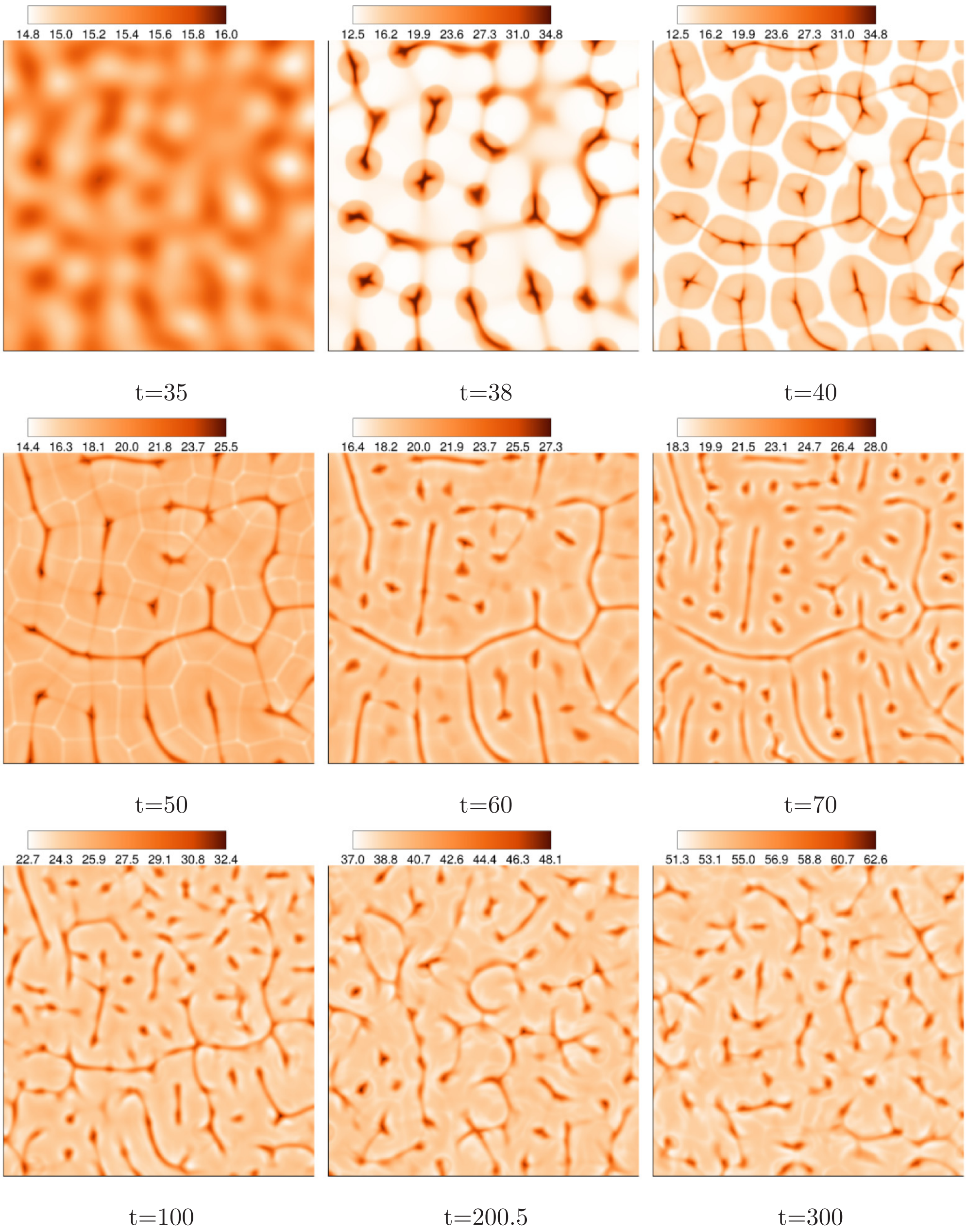

t=35 t=38 t=40

t=50 t=60 t=70

t=100 t=200.5 t=300

FIG. 9. (Color online) Plots of $\bar{A}(x,y,t)$ for different times in 3D simulations for type II. A subdomain domain $(x,y) \in [0,8] \times [0,8]$ is shown. Dark areas correspond to high values = max(A) "downwelling curtains" and bright areas = min(A) correspond to upwelling lighter fluid. At any time the color is adjusted to the minimum and maximum values.

(Fig. 12). It occurs by a continuous growth of larger cells as well as by the inclusion of smaller cells into larger ones. In relatively low acid concentration (light regions in Fig. 12), fluid rises to the interface and absorbs oxygen from the air layer. The oxygen gradient $\partial_z\Omega(x,y,z=1,t)$ and the vertically averaged methylene-blue concentration $\bar{B}(x,y,t)$ (Fig. 11) indicate that (a) oxygen-rich fluid gets denser by the two reaction steps and sinks down with enriched acid in the boundaries of the polygonal cells and (b) upwelling fluid, free of oxidized methylene B, takes up oxygen [dark green (dark gray)] at the interface, is enriched in B, and sinks subsequently [dark blue (dark gray)].

In the range $50 < t < 200$ a considerable growth is observed in the characteristic length scales, quantified by the wavelength $2\pi/k^A$ in Fig. 13(a). From time $t = 200$ onward, the maximum mode $2\pi/k^A_{\text{max}}$ corresponds to the edge length of the domain. The cell size is thus limited by the finite horizontal domain size equal to 20. Note that the rms velocity $U = \sqrt{\langle \mathbf{u}\cdot\mathbf{u}\rangle_{xyz}}$ [see Fig. 13(b)] almost saturates at $t = 200$. Figure 13(c) displays the maximum acid concentration differences on the surface $\Delta A(t) = \max_{xy}\{A(z=1,x,y)\} - \min_{xy}\{A(z=1,x,y)\}$. It increases with time; however, its growth is also decelerated from $t = 200$ onward. The convection pattern finally arrives at one large convection cell around

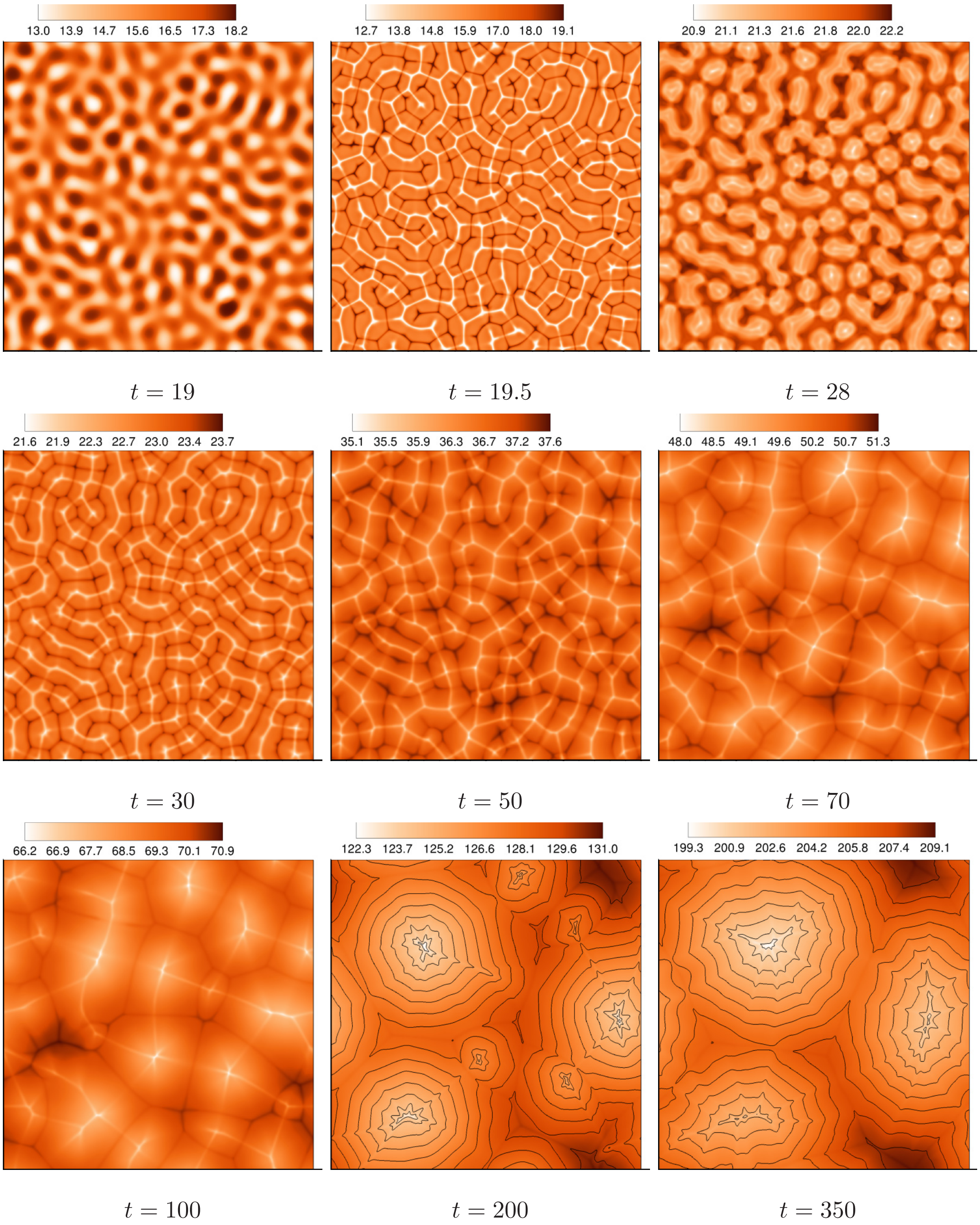

$t = 19$ $t = 19.5$ $t = 28$

$t = 30$ $t = 50$ $t = 70$

$t = 100$ $t = 200$ $t = 350$

FIG. 10. (Color online) Plots of $\bar{A}(x,y,t)$ in 3D simulations for type I. The full domain $(x,y) \in [0,20] \times [0,20]$ is shown. Dark areas correspond to high values $= \max(\bar{A})$ "downwelling curtains" and bright areas $= \min(\bar{A})$ correspond to upwelling lighter fluid. At any time the color is adjusted to the minimum and maximum values. Isolines are included for the latest times.

$t = 700$. This is not shown in Fig. 13, where the largest time is $t = 400$.

The features of the type I experiment are peculiar compared to the standard Rayleigh-Bénard convection. Howard [41] viewed the turbulent Rayleigh-Bénard regime as a cyclic growth and disruption of an unstably stratified layer near boundaries. These layers are generated by the diffusion of heat and do not depend on velocity. For type I experiments, the viscous time is smaller than reaction time scale. In that case, the size and velocity of the convection cells distinctly impacts the density differences near the upper boundary through the turnover time of convection cells.

For type II or type III, the reaction time scale governs how the upper unstably stratified layer is produced: The unstably stratified layer depends on diffusion of oxygen and reaction rates.

2. Dripping flow regime: Types II and III

Type I displays coarsening. By contrast, types II and III develop a structure characterized by localized plume emissions. As mentioned above, the change of the flow regime (compared to type I) might be related to $T_{\mathrm{vis}} > T_{\mathrm{reac}}$ for type II. In the following we concentrate on type II only since type III is qualitatively similar. The instantaneous flow structure

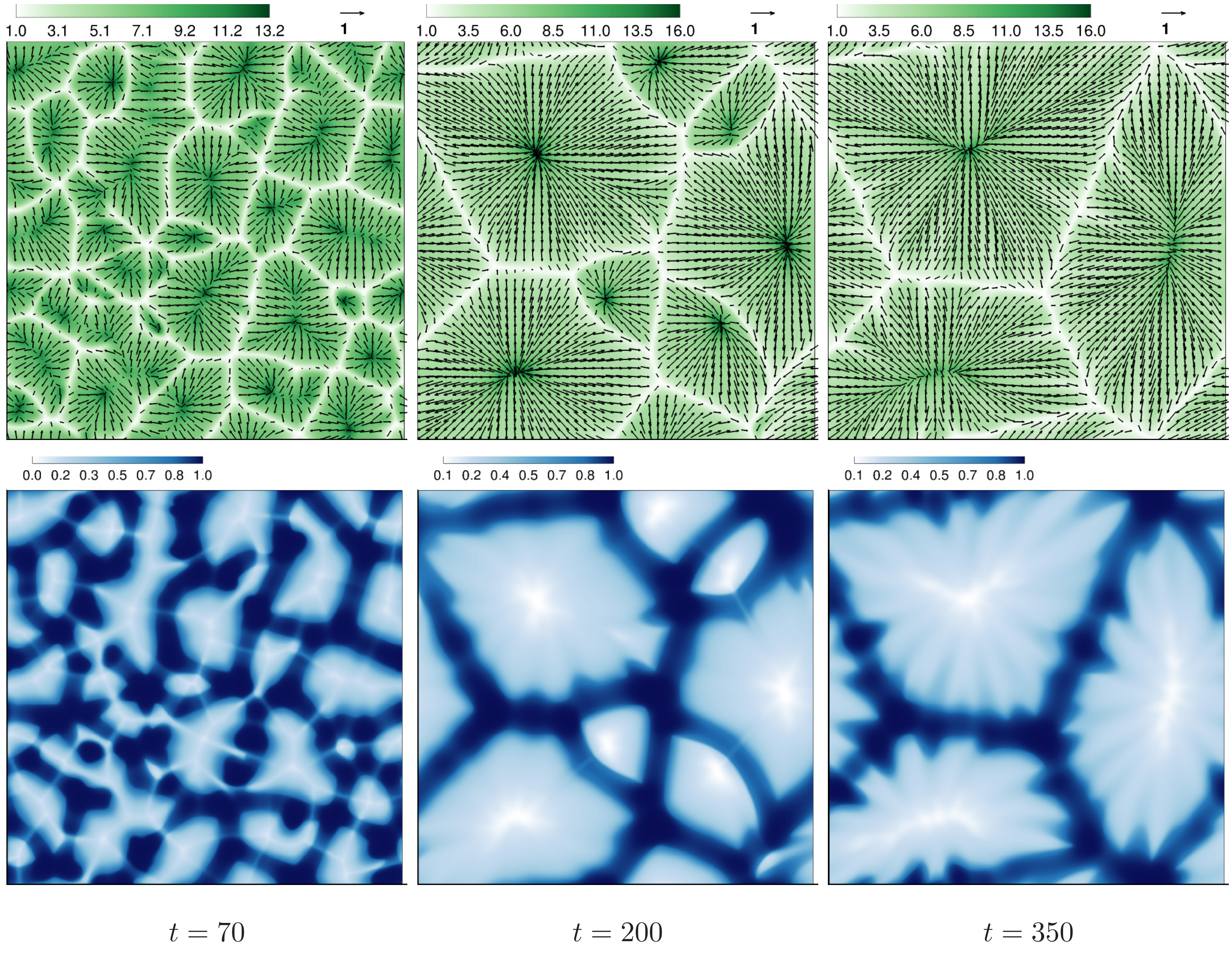

$t = 70$ $t = 200$ $t = 350$

FIG. 11. (Color online) Three-dimensional simulations for type I: Plots of $\partial_z \Omega(x,y,z = 1,t)$ (top) and $\bar{B}(x,y,t)$ (bottom) for different times in full numerical domain $(x,y) \in [0.20] \times [0,20]$ (black areas = high value, light gray = low value). The arrows in the top row represent the velocity field at the surface $z = 1$.

is shown in Fig. 14 together with the oxygen gradient at the interface $\partial_z \Omega(x,y,z = 1)$, the methylene blue $\bar{B}(x,y,t)$, and acid $\bar{A}(x,y,t)$ patterns. In addition, a vertical cross section with acid concentration and tangential velocity field is displayed in Fig. 15.

Starting with the pattern observed at onset (Fig. 9), the flow rearranges for $t > 100$ into a statistically stationary state: Convection rolls (appearing as dark stripes) are disrupted by descending solutal plumes (appearing as dots). The main driving mechanism is the same as in type I, i.e., upwelling fluid adsorbs oxygen at the interface and sinks down but now in smaller and individually unsteady convective structures. Length scales are smaller relative to type I and they are not growing [see the wavelength $\lambda_A = 2\pi/k^A_{\text{avg}}$ in Fig. 16(a)].

For times $t > 100$, the system reaches a statistically steady state as documented by the wavelength $\lambda_A = 2\pi/k^A_{\text{avg}}$ and the velocity measure $\sqrt{\langle \mathbf{u} \cdot \mathbf{u} \rangle_{xyz}}$ (see Fig. 16). In this regime, the finger and plume structures are constantly evolving as seen in the space time plot of the acid concentration at the interface (see Fig. 17) where the source of downwelling dense liquid can be traced by the continuous dark areas that are high in concentration. We call this flow a *dripping* regime. A characteristic time scale for pattern decorrelation can be obtained by computing an autocorrelation function $\langle \bar{A}(t)\bar{A}(t+\tau)\rangle_{xy}$. It is evaluated (not shown) to be of the order of the convective time $\lambda_A/\sqrt{\langle \mathbf{u} \cdot \mathbf{u} \rangle_{xyz}} = 11.23$ based on the pattern length scale λ_A and velocity $\sqrt{\langle \mathbf{u} \cdot \mathbf{u} \rangle_{xyz}}$ of Fig. 16.

C. Comparison with former simulations

The two-dimensional simulations of Pons *et al.* [31] focused on type I experiments. In these simulations, the air layer is neglected and a boundary condition on oxygen concentration is used. Our simulations show that the oxygen concentration at the interface (in the liquid phase) differs very weakly from the averaged concentration in the air layer divided by Henry's constant: The standard deviation $\langle [\langle \Omega^{\text{air}} \rangle_{xyz}/c_H - \Omega(x,y,z = 1)]^2 \rangle_{xy}^{1/2}$ is distinctly below 10^{-4} for the simulated times of

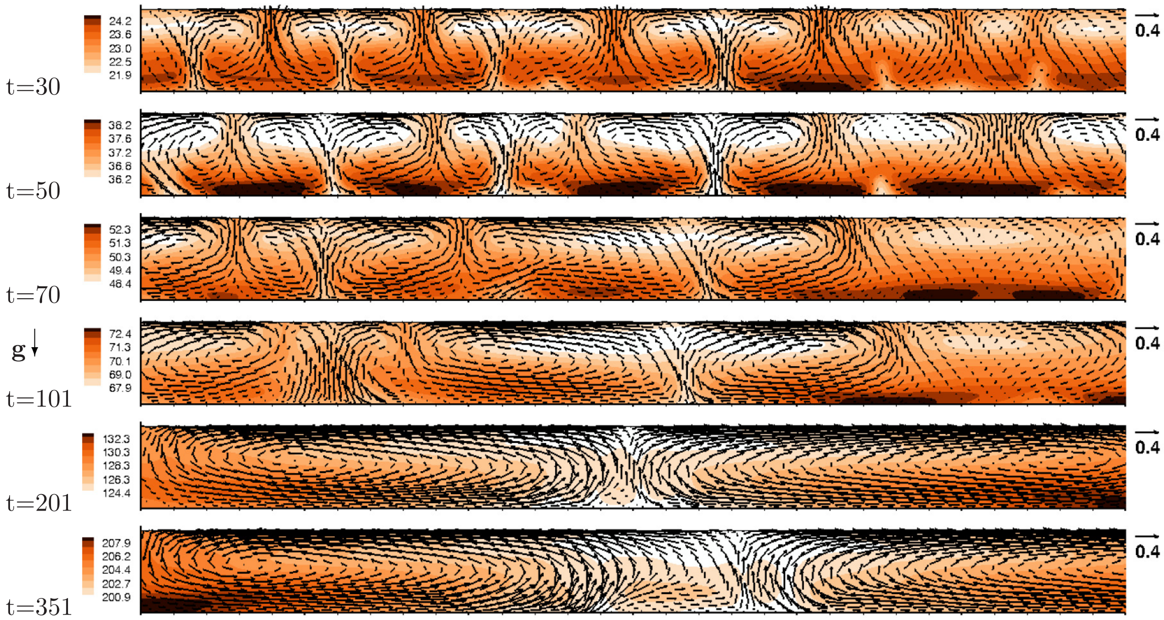

FIG. 12. (Color online) Three-dimensional simulations for type I: Plots of $A(x,y=15,z,t)$ at constant $y=15$ for $x \in [0,12]$, $z \in [0,1]$ and different times. The arrows represent the velocity field tangential to the plane.

nonlinear simulation. Consequently, the upper air layer can be accurately modeled by a fixed concentration boundary condition,

$$\Omega(x,y,z=1) = \langle \Omega^{\mathrm{air}} \rangle_{xyz} / c_H. \qquad (35)$$

Simulations of Pons *et al.* [31] show a behavior similar to ours apart from the wall influence: Onset time around $t=18$, an initial damped oscillation in methylene-blue amplitude [cf. Fig. 5(a)], and a subsequent coarsening are also observed there [31]. However, walls can lead to a large-scale shear flow through the full domain at late times [see Ref. [31], Fig. 7(b)].

D. Comparison with former experiment

The experiments [29] were conducted in a Petri dish of 18.5-cm diameter. The pattern was observed via the light adsorption of methylene blue in a rectangular window of 12.4-cm width with 256 pixels and, for a smaller box height, 192 pixels (y range). By this the vertical average of methylene blue $\bar{B}(x,y,t)$ is recorded, assuming that the Beer-Lambert's law holds for methylene blue. The main experimental results that have been reported describe the onset time, the dominant wave-number evolution, and some characteristic patterns for different experimental conditions. Pons *et al.* [29] divided the experimental evolution into three phases: linear growth, nonlinear saturation (our onset phase), and a third phase which shows different behaviors with experimental conditions, i.e., decreasing, constant, or oscillating wave numbers (cf. Figs. 9, 12, and 13 in Ref. [29]). This third phase ends with the disappearance of the pattern. Such behaviors are also seen in our simulations except for the disappearance of the patterns, which is not predicted by the present model.

Let us first compare the onset time of convection and the initial dominant wave number (see Table III). For experiment 12 (type I), the onset is at $T_{\mathrm{onset}}^{\mathrm{exp12}} = 11.16$ with

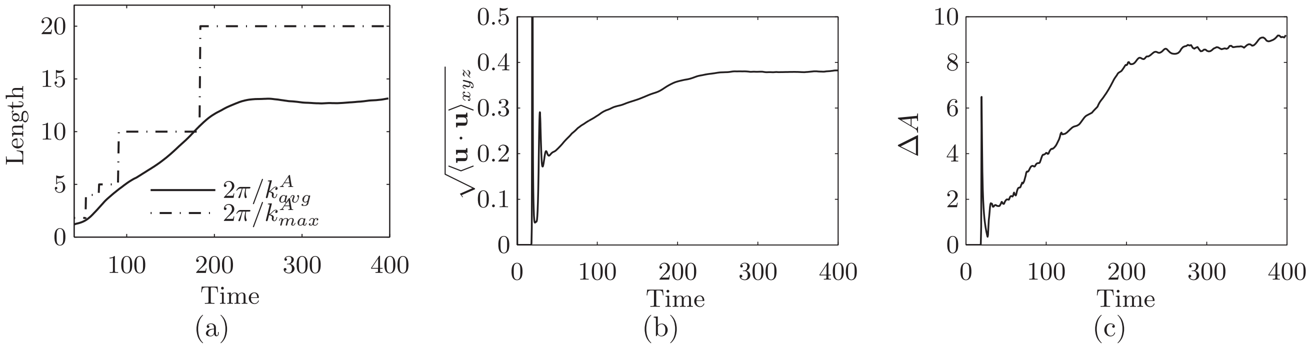

(a) (b) (c)

FIG. 13. Three-dimensional simulations for type I. (a) Dominate wavelengths of $\bar{A}(x,y,t)$, (b) root-mean-squared velocity, and (c) maximum acid differences at the interface.

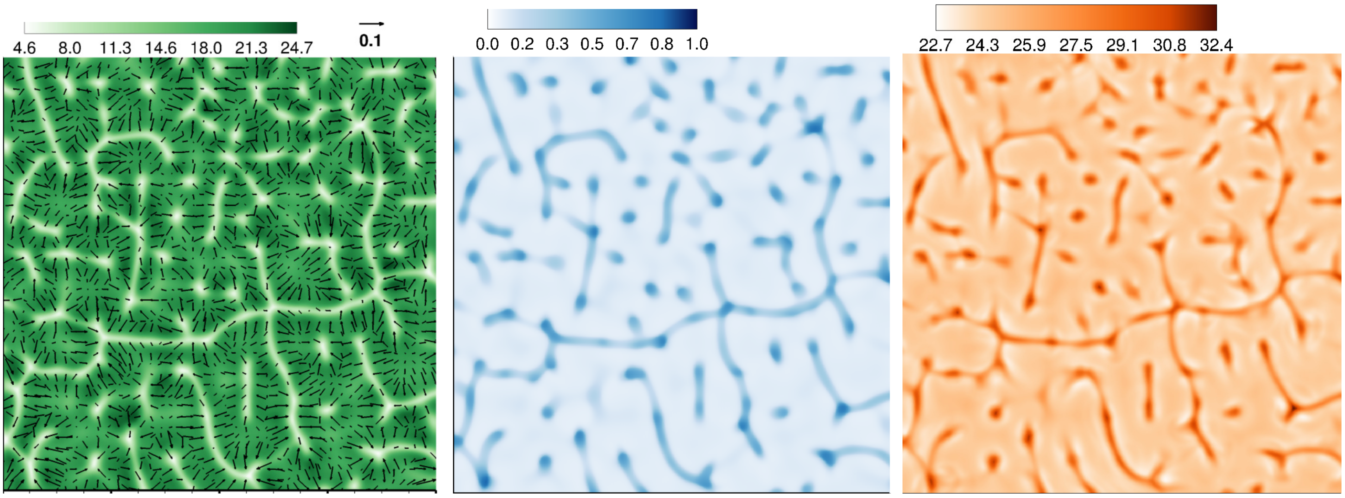

$\partial_z\Omega(x,y,z=1,t=100)$ $\bar{B}(x,y,t=100)$ $\bar{A}(x,y,t=100)$

FIG. 14. (Color online) Three-dimensional simulations for type II in subdomain $(x,y) \in [0,8] \times [0,8]$: $\partial_z\Omega(x,y,z=1,t)$ (left), $\bar{B}(x,y,t=100)$ (center), and $\bar{A}(x,y,t=100)$ (right) (black areas, high value; light gray, low value; the colors are adapted to the extreme values). The arrows represent the velocity field at the surface $z = 1$.

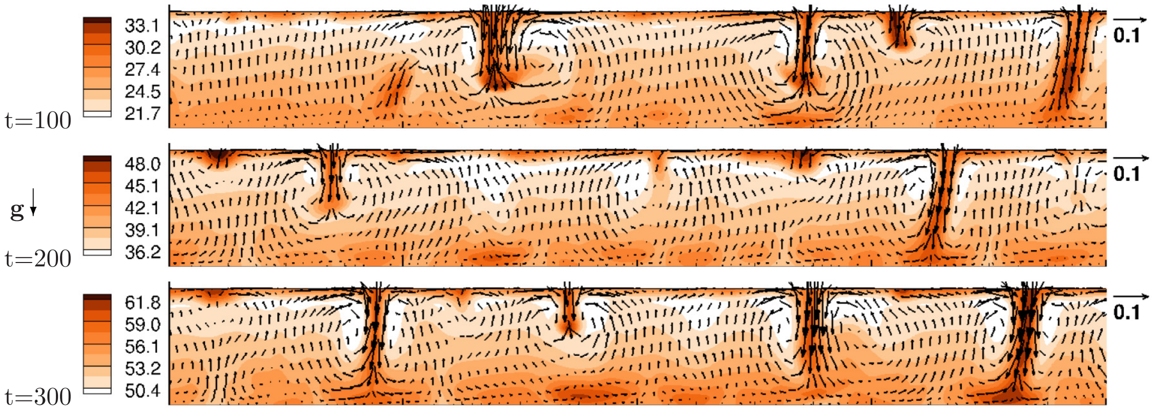

FIG. 15. (Color online) Three-dimensional simulations for type II statistically steady state $t \geqslant 100$: Plots of $A(x,y,z,t)$ at constant $y = 15$, $x \in [0,8]$ for different times in a simulation. The arrows represent the tangential velocity field with a reference arrow at the right side.

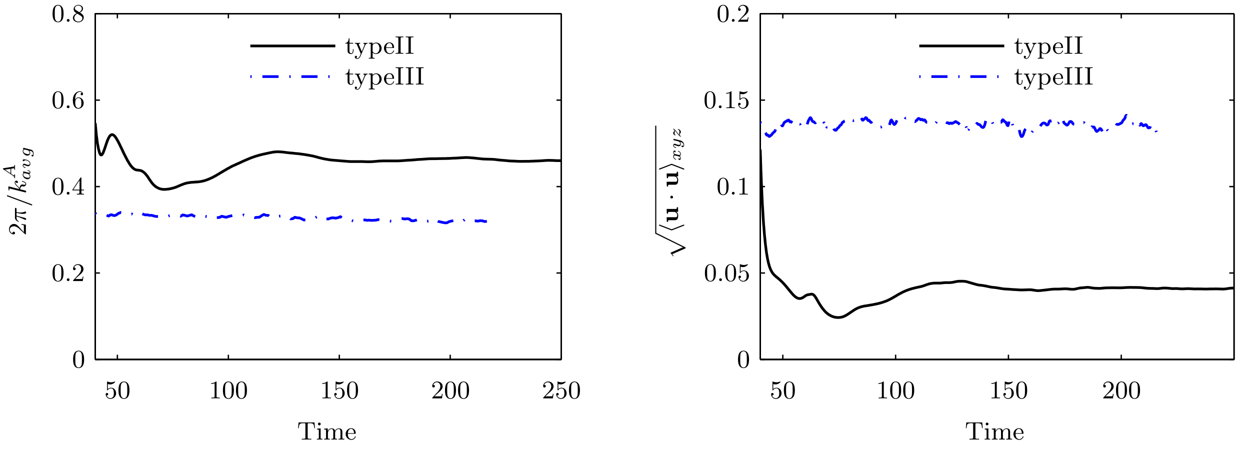

(a) (b)

FIG. 16. (Color online) Three-dimensional simulations in dribbling flow regime for types II and III. (a) Dominant length $\lambda_A = 2\pi/k^A_{\text{avg}}$ in acid patterns; (b) rms velocity. Sample values extracted at $t = 200$ are $\sqrt{\langle \mathbf{u}\cdot\mathbf{u}\rangle_{xyz}}^{\text{II}} = 0.0414$, $\lambda^{\text{II}}_A = 0.465$, $\sqrt{\langle \mathbf{u}\cdot\mathbf{u}\rangle_{xyz}}^{\text{III}} = 0.137$, and $\lambda^{\text{III}}_A = 0.319$.

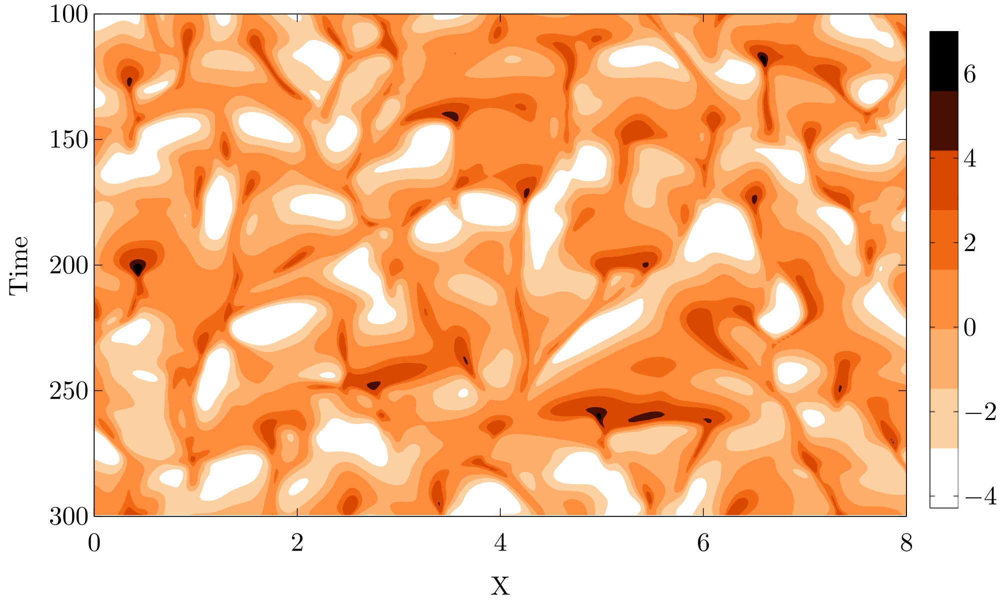

FIG. 17. (Color online) Type II in the statistically steady regime: Space-time plots of the interface concentration $A(x,y=15,z=1,t) - \langle A(x,y,z=1,t)\rangle_{xy}$ at constant $y=15$, $x \in [0,8]$ for times $t \in [100,300]$.

wave number $\alpha_{\text{onset}}^{\text{exp12}} = 3.85$. It occurs before the earliest prediction of the linear stability analysis based on the E_A objective function, i.e., $T_c = 12.5$ with wave number $\alpha_c = 2.8$. For velocity perturbations, which are practically present when pouring the mixture into the Petri dish, the difference is even higher higher: $T_c = 18.2$ ($\alpha_c = 3.6$). For experiment 7 (type II), the onset time $T_{\text{onset}}^{\text{exp7}} = 17.06$ with $\alpha_{\text{onset}}^{\text{exp7}} = 8.51$ is reported which is between the critical time obtained using the acid perturbation (function E_A) $T_c = 14.8$ ($\alpha_c^A = 3.85$) and the velocity perturbation (function E_k) $T_c = 34.2$ ($\alpha_c = 4.5$). Experimental onset times decrease with increased liquid layer depth. This trend is reproduced by calculations for type III, which show the earliest onset times $T_c^A = 11.1$.

During evolution, the dominant wave-number progression for experiments 7 and 12 is extracted from Ref. [29] and plotted together with the data from the respective simulation in Fig. 18. The numerical trend of higher wave numbers for type II relative to type I is in accordance with experiments; however, there is a gap between experiment and simulation. The visual appearance of the methylene-blue patterns from Ref. [29] shares general features but differs in some points. For experiment 12 (type I), a short coarsening phase is observed (see Fig. 1 in Ref. [29]), but the experimental pattern then disappears preferentially at the walls around $t = 60$. For type II, a tendency towards more stripes in the experimental pattern is seen (see Fig. 7 in Ref. [29]), in accordance with simulations. The tendency to lines or stripes rather than dots

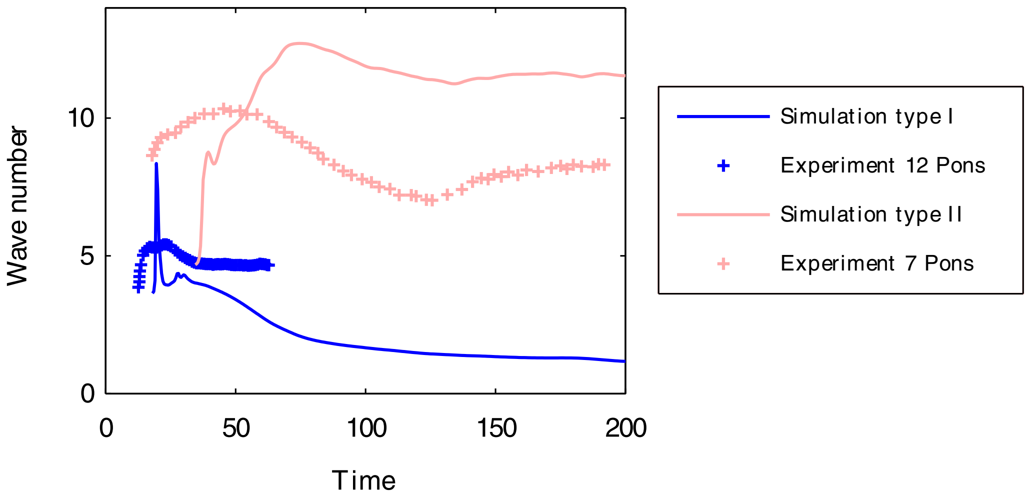

FIG. 18. (Color online) Comparison of simulated wave numbers k_{avg}^B with experimental data extracted from Ref. [29] while type I refers to experiment 12 and type II to experiment 7.

for systems with a larger layer depths, as in type III, is also pointed out in Ref. [29].

The discrepancy between simulation and experiment may have two main origins: deficiencies in the chemical model [28] and variability of experimental conditions. More specifically, the chemical model developed in Ref. [28] needs to be extended to capture the final disappearance of the convection patterns observed in Ref. [29]. Thus additional conservation equations would have to be included for glucose and NaOH, which are absent from the present reaction scheme. The influence of these species on reaction rates would also have to be modeled. A related discussion can be found in Ref. [42]. Our study also suggests that the initial evolution of the system (especially onset time of convection) is sensitive to the initial state (see Table III and Fig. 4). This point could be clarified by repeating the experiments under the same conditions and recording deviations among them.

Another possible cause for discrepancies are the vertical walls in the experiments: Although initially the experimental patterns appeared periodic, the wall influence becomes apparent in Fig. 1 of Ref. [29], where the pattern of experiment 12 (type I) starts to disappear from the walls. Furthermore, the two-dimensional simulation [31] suggests that the walls may lead to a large-scale flow, which may cause large radial stripes of methylene blue ranging from the wall to the center of the Petri dish, see Fig. 1(b) in Pons *et al.* [31].

IX. CONCLUSION

We have numerically studied the chemohydrodynamic convection of methylene-blue–glucose based on the model proposed by Bees *et al.* [28]. In the present study, this model has been extended to a closed system: An air layer is included where oxygen is transported by diffusion and the concentration jump of oxygen at the interface between liquid and air is governed by Henry's law.

To characterize convection onset, a non-normal stability analysis was performed that revealed the dependence of onset time and dominant wave numbers on initial perturbations. The system is much more sensitive to perturbations in the concentration fields than to perturbations located in the velocity field. We further studied the convection onset by using a fully three-dimensional nonlinear model with velocity perturbation for three different experimental conditions. The onset time of convection decreases logarithmically with the initial perturbation amplitude both for random and optimal initial perturbations.

In a second part, the nonlinear evolution of the three-dimensional runs was shown for large periodic boxes. These runs correspond to three different experimental types. The first convection phase proceeds similar for the three cases. The unstable layer of gluconic acid at the air-liquid interface is entrained in plumelike structures into the bulk. However, the subsequent flow regimes change considerably for the three cases.

Type I showed a flow regime which is marked by a steady increase in the size of flow structures until the length scale of the convection cells is comparable to the system size. The coarsening proceeds as large convection cells continuously increases in size and absorb smaller cells in their vicinity. Generally, convection occurs in a low-Reynolds-number regime.

The *dripping flow regime* of types II and III is marked by downwelling dense liquid that is localized in a convective structure of short lifetime. In contrast to the type I regime, the buildup of unstable acid layers is less coupled to the downwelling liquid. This change is explained by the fact that the time of viscous equilibration is larger than reactive time scale.

The comparison of our results with former experimental studies showed the need for further combined experimental and numerical work to improve physical modeling (chemistry, air-liquid interface combined with the vertical walls) for the methylene-blue–glucose system.

ACKNOWLEDGMENTS

Financial support by the Deutsche Forschungsgemeinschaft in the framework of Priority Program 1506 (Grant No. Bo1668/6) is gratefully acknowledged. Furthermore, we thank the computing center (UniRZ) of TU Ilmenau and FZ Jülich (NIC) for access to its parallel computing resources. Finally, we thank Dmitry Krasnov for fruitful discussions and comments.

APPENDIX A: TRANSIENT LINEAR STABILITY METHOD

1. Basic evolution

A possible solution to the governing equations is an unsteady pure diffusion-reaction process, in which concentrations evolve along z only and the velocity field remains zero,

$$\mathbf{u} = 0, \quad A = A_0(z,t), \quad B = B_0(z,t), \quad \Omega = \Omega_0(z,t),$$
$$P = P_0(z,t), \quad \Omega^{\mathrm{air}} = \Omega_0^{\mathrm{air}}(z,t). \tag{A1}$$

Introducing (A1) into Eq. (3) provides an equation for the pressure as follows:

$$\frac{\partial P_0}{\partial z} + \delta_d R A_0(z,t) = 0. \tag{A2}$$

From Eqs. (5) to (8), and boundary conditions (11) to (14), one obtains the following set of equations governing the basic state:

$$\frac{\partial A_0}{\partial t} = \frac{\delta_A}{\delta_d^2}\frac{\partial^2 A_0}{\partial z^2} + B_0, \tag{A3}$$

$$\frac{\partial B_0}{\partial t} = \frac{1}{\delta_d^2}\frac{\partial^2 B_0}{\partial z^2} + \kappa\Omega_0(1 - B_0) - B_0, \tag{A4}$$

$$\frac{\partial \Omega_0}{\partial t} = \frac{\delta_\Omega}{\delta_d^2}\frac{\partial^2 \Omega_0}{\partial z^2} - \lambda\Omega_0(1 - B_0), \tag{A5}$$

$$\frac{\partial \Omega_0^{\mathrm{air}}}{\partial t} = \frac{\delta_{\mathrm{air}}}{\delta_d^2\delta_l^2}\frac{\partial^2 \Omega_0^{\mathrm{air}}}{\partial \xi^2}. \tag{A6}$$

Note that the dimensional vertical coordinate in the air layer $\tilde{z} \in [d, d + l]$ is transformed by $\xi = (\tilde{z} - d)/l$. This is done in all equations in the Appendix in order to consider the dimensionless coordinate z,ξ from the interval $[0,1]$ only. The boundary conditions are as follows:

$$\frac{\partial A_0}{\partial z} = \frac{\partial B_0}{\partial z} = \frac{\partial \Omega_0}{\partial z} = 0 \quad \text{at } z = 0, \tag{A7}$$

$$\begin{gathered}\frac{\partial A_0}{\partial z} = \frac{\partial B_0}{\partial z} = 0; \quad \frac{\partial \Omega_0^{\rm air}}{\partial z} = 0 \\ \text{at } z = 1, \text{ respectively}, \xi = 1,\end{gathered} \tag{A8}$$

$$\frac{\partial \Omega_0(z=1)}{\partial z} = \frac{\delta_{\rm air}}{\delta_l \delta_\Omega} \frac{\partial \Omega_0^{\rm air}(\xi = 0)}{\partial \xi}, \tag{A9}$$

$$\Omega_0(z=1) = \Omega_0^{\rm air}(\xi = 0)/c_H. \tag{A10}$$

2. Linear perturbation equations

The solution of the full governing Eqs. (3) to (8) is split into the basic state and perturbations. The perturbations are assumed of weak amplitude and therefore any term higher than linear in perturbations is neglected. The linear system on $z,\xi \in [0,1]$ reads

$$\frac{\delta_d^2}{\rm Sc} \frac{\partial \hat{u}}{\partial t} + i\alpha \hat{p} - \left[\frac{\partial^2}{\partial z^2} - \alpha^2\right]\hat{u} = 0, \tag{A11}$$

$$\frac{\delta_d^2}{\rm Sc} \frac{\partial \hat{w}}{\partial t} + \frac{\partial \hat{p}}{\partial z} - \left[\frac{\partial^2}{\partial z^2} - \alpha^2\right]\hat{w} + \delta_d R \hat{A} = 0, \tag{A12}$$

$$\begin{aligned}&\frac{\partial \hat{A}}{\partial t} + i\alpha A_0 \hat{u} + \frac{\partial (A_0 \hat{w})}{\partial z} - \frac{\delta_A}{\delta_d^2}\left[\frac{\partial^2}{\partial z^2} - \alpha^2\right]\hat{A} - \hat{B} = 0, \\ &\frac{\partial \hat{B}}{\partial t} + i\alpha B_0 \hat{u} + \frac{\partial (B_0 \hat{w})}{\partial z} - \frac{1}{\delta_d^2}\left[\frac{\partial^2}{\partial z^2} - \alpha^2\right]\hat{B} \\ &\quad + \kappa \Omega_0 \hat{B} - \kappa \hat{\Omega}(1 - B_0) + \hat{B} = 0,\end{aligned} \tag{A13}$$

$$\begin{aligned}&\frac{\partial \hat{\Omega}}{\partial t} + i\alpha \Omega_0 \hat{u} + \frac{\partial (\Omega_0 \hat{w})}{\partial z} - \frac{\delta_\Omega}{\delta_d^2}\left[\frac{\partial^2}{\partial z^2} - \alpha^2\right]\hat{\Omega} \\ &\quad - \lambda \Omega_0 \hat{B} + \lambda \hat{\Omega}(1 - B_0) = 0,\end{aligned} \tag{A14}$$

$$\frac{\partial \hat{\Omega}^{\rm air}}{\partial t} - \frac{\delta_{\rm air}}{\delta_d^2 \delta_l^2}\left[\frac{\partial^2}{\partial \xi^2} - \alpha^2\right]\hat{\Omega}^{\rm air} = 0, \tag{A15}$$

$$i\alpha \hat{u} + \frac{\partial \hat{w}}{\partial z} = 0, \tag{A16}$$

and boundary conditions

$$\hat{w} = \frac{\partial^2 \hat{w}}{\partial z^2} = 0 \qquad \text{at } z = 1, \tag{A17}$$

$$\hat{w} = \frac{\partial \hat{w}}{\partial z} = 0 \qquad \text{at } z = 0, \tag{A18}$$

$$\frac{\partial \hat{A}}{\partial z} = \frac{\partial \hat{B}}{\partial z} = \frac{\partial \hat{\Omega}^{\rm air}}{\partial z} = 0 \qquad \text{at } z = 1, \tag{A19}$$

$$\frac{\partial \hat{A}}{\partial z} = \frac{\partial \hat{B}}{\partial z} = \frac{\partial \hat{\Omega}}{\partial z} = 0 \qquad \text{at } z = 0, \tag{A20}$$

$$\frac{\partial \hat{\Omega}(z=1)}{\partial z} = \frac{\delta_{\rm air}}{\delta_l \delta_\Omega} \frac{\partial \hat{\Omega}^{\rm air}(\xi = 0)}{\partial \xi}, \tag{A21}$$

$$\hat{\Omega}(z=1) = \hat{\Omega}^{\rm air}(\xi = 0)/c_H. \tag{A22}$$

APPENDIX B: OPTIMIZATION PROCEDURE

We continue the presentation of Sec. VI A, where we stated the optimization problem in terms of the objective functions $E_\beta(\mathbf{q})$. We therefore construct a Langragian function by

$$\begin{aligned}L(\mathbf{q},\tilde{\mathbf{q}},s_0,T) &= E_\beta(\mathbf{q}(T)) - s_0[E_\beta(\mathbf{q}(0)) - 1] \\ &\quad - \sum_{j=1}^{7} \int_0^T dt(\langle F_j(\mathbf{q}(t)),\tilde{q}_j(t)\rangle_2) + (\text{c.c.}).\end{aligned} \tag{B1}$$

The first term $E_\beta(\mathbf{q}(T))$ is the objective function, which is to be maximized at time T. The second term in Eq. (B1) enforces the normalization to unity of the initial perturbation with the Lagrangian mulipliers s_0. The third term enforces the linear governing equations, where F_j is the left-hand side of Eqs. (A11) to (A16) and $\tilde{\mathbf{q}}$ is the Lagrangian multipliers field. The abbreviation c.c. denotes complex conjugate of $\langle F_j(\mathbf{q}(t)),\tilde{\mathbf{q}}_j(t)\rangle_2$ and $\langle \cdot,\cdot \rangle_2$ stands for the L_2 scalar product,

$$\langle a_1,a_2\rangle_2 \equiv \int \hat{a}_1(z)\hat{a}_2^*(z)dz. \tag{B2}$$

An extremum of $E_\beta(\mathbf{q}(T))$ is found if the first variation of L is zero,

$$\delta L = \frac{dL(\mathbf{q} + h\delta\mathbf{q})}{dh}\Big|_{h=0} = 0, \tag{B3}$$

with respect to the test functions $\delta\mathbf{q}$. The sum $\mathbf{q} + h\delta\mathbf{q}(z,t)$ has to admit the initial and boundary conditions as well as the governing equations. In this case, $L = E$ and $\delta L = \delta E$.

Starting with Eq. (B3) we derive a complete set of governing equations to compute the Lagrangian multipliers. For a given wave number α, objective function E_β, and time T, the field $\mathbf{q}$ satisfying Eq. (B3) is called optimal perturbation $\mathbf{q}_{\rm opt}$. Note that we do not distinguish between the coordinates in the upper ξ and the lower layer z and just write "z" as they pass trough the same range of real numbers.

The Lagrangian multipliers fields correspond to the following adjoint fields: $\tilde{u}(z,t)$, $\tilde{w}(z,t)$, $\tilde{A}(z,t)$, $\tilde{B}(z,t)$, $\tilde{\Omega}(z,t)$, $\tilde{\Omega}^{\rm air}(z,t)$, $\tilde{p}(z,t)$, while s_0 is just a real number.

The calculation of the optimal perturbation relies on the examination of Eq. (B3) to obtain the Lagrangian multipliers, and it reads

$$\begin{aligned}\delta L &= \sum_{j=1}^{5} C_j \left(\int q_j^*(z,T)\delta q_j(z,T)dz\right) \\ &\quad - s_0 \sum_{j=1}^{5} \left(\int q_j^*(z,0)\delta q_j(z,0)dz\right) \\ &\quad \underbrace{- \sum_{j=1}^{7} \int_0^T dt[\langle \delta F_j(\mathbf{q}(t))\tilde{q}_j(t)\rangle_2}_{I} \\ &\quad + \langle F_j(\mathbf{q}(t)),\delta\tilde{q}_j(t)\rangle_2] + (\text{c.c.}).\end{aligned} \tag{B4}$$

The integral $\langle F_j(q(t)),\delta\tilde{q}_j(t)\rangle_2$ in Eq. (B4) is zero if the governing equations $F_j(\mathbf{q}) = 0$ are satisfied during the time interval $[0,T]$. The main idea then amounts to rewriting quantity $\langle \delta F_j(q(t)),\tilde{q}_j(t)\rangle_2$ in terms of $\delta q_k(t)$ by partial integration, which gives a system of PDEs for the Lagrangian multiplier $\tilde{\mathbf{q}}$. Including all boundary and initial condition in the partial integration process and changing the sign of the time coordinate $\tau = -t$, one obtains the following adjoint system:

$$\frac{\delta_d^2}{\mathrm{Sc}}\frac{\partial\tilde{u}}{\partial\tau} - i\alpha\tilde{p} - \left[\frac{\partial^2}{\partial z^2} - \alpha^2\right]\tilde{u} - i\alpha(A_0\tilde{A} + B_0\tilde{B} + \Omega_0\tilde{\Omega}) = 0, \tag{B5}$$

$$\frac{\delta_d^2}{\mathrm{Sc}}\frac{\partial\tilde{w}}{\partial\tau} - \frac{\partial\tilde{p}}{\partial z} - \left[\frac{\partial^2}{\partial z^2} - \alpha^2\right]\tilde{w} - \left(A_0\frac{\partial\tilde{A}}{\partial z} + B_0\frac{\partial\tilde{B}}{\partial z} + \Omega_0\frac{\partial\tilde{\Omega}}{\partial z}\right) = 0, \tag{B6}$$

$$\frac{\partial\tilde{A}}{\partial\tau} - \frac{\delta_A}{\delta_d^2}\left[\frac{\partial^2}{\partial z^2} - \alpha^2\right]\tilde{A} + \delta_d R\tilde{w} = 0, \tag{B7}$$

$$\frac{\partial\tilde{B}}{\partial\tau} - \frac{1}{\delta_d^2}\left[\frac{\partial^2}{\partial z^2} - \alpha^2\right]\tilde{B} + (\kappa\Omega_0 + 1)\tilde{B} - \lambda\Omega_0\tilde{\Omega} - \tilde{A} = 0, \tag{B8}$$

$$\frac{\partial\tilde{\Omega}}{\partial\tau} - \frac{\delta_\Omega}{\delta_d^2}\left[\frac{\partial^2}{\partial z^2} - \alpha^2\right]\tilde{\Omega} + (1 - B_0)(\lambda\tilde{\Omega} - \kappa\tilde{B}) = 0, \tag{B9}$$

$$\frac{\partial\tilde{\Omega}^{\mathrm{air}}}{\partial\tau} - \frac{\delta_{\mathrm{air}}}{\delta_d^2\delta_l^2}\left[\frac{\partial^2}{\partial z^2} - \alpha^2\right]\tilde{\Omega}^{\mathrm{air}} = 0, \tag{B10}$$

$$i\alpha\tilde{u} + \frac{\partial\tilde{w}}{\partial z} = 0. \tag{B11}$$

Using the boundary conditions of the system, the analogous boundary conditions are derived from the partial integration procedure to the following:

$$\tilde{u} = \frac{\partial\tilde{w}}{\partial z} = \tilde{w} = 0 \qquad \text{at } z = 0, \tag{B12}$$

$$\tilde{w} = \frac{\partial\tilde{u}}{\partial z} = \frac{\partial^2\tilde{w}}{\partial z^2} = 0 \qquad \text{at } z = 1, \tag{B13}$$

$$\frac{\partial\tilde{A}}{\partial z} = \frac{\partial\tilde{B}}{\partial z} = \frac{\partial\tilde{\Omega}}{\partial z} = 0 \qquad \text{at } z = 0, \tag{B14}$$

$$\frac{\partial\tilde{A}}{\partial z} = \frac{\partial\tilde{B}}{\partial z} = \tilde{\Omega}^{\mathrm{air}} = 0 \qquad \text{at } z = 1, \tag{B15}$$

$$\delta_l\tilde{\Omega}^{\mathrm{air}}(z=0) = \tilde{\Omega}(z=1), \tag{B16}$$

$$\frac{\delta_\Omega\delta_l^2}{\delta_{\mathrm{air}}c_H}\frac{\partial\tilde{\Omega}^{\mathrm{air}}(z=0)}{\partial z} = \frac{\partial\tilde{\Omega}(z=1)}{\partial z}. \tag{B17}$$

Depending on what objective functions E_β is used the terminal condition for the adjoint and direct fields change, which is just a consequence on demanding the first two terms being zero in Eq. (B4). For instance, the velocity case E_k demands

$$\hat{u}(T)\mathrm{Sc} = \tilde{u}(T),\ \hat{w}(T)\mathrm{Sc} = \tilde{w}(T), \tag{B18}$$

$$\tilde{A}(T) = \hat{A}(0) = \tilde{B}(T_e) = \hat{B}(0) = \tilde{\Omega}(T) = 0, \tag{B19}$$

$$\hat{\Omega}(0) = \tilde{\Omega}^{\mathrm{air}}(T) = \hat{\Omega}^{\mathrm{air}}(0) = 0, \tag{B20}$$

$$\hat{u}(0) = \frac{\tilde{u}(0)}{s_0\mathrm{Sc}},\ \hat{w}(0) = \frac{\tilde{w}(0)}{s_0\mathrm{Sc}}. \tag{B21}$$

The value of s_0 is chosen as

$$s_0 = \sqrt{E_k\left(\frac{1}{\mathrm{Sc}}\tilde{\mathbf{q}}(0)\right)}. \tag{B22}$$

This choice, included in condition (B21), yields

$$\hat{u}(0) = \frac{\tilde{u}(0)}{\sqrt{E_k(\tilde{\mathbf{q}}(0))}},\ \hat{w}(0) = \frac{\tilde{w}(0)}{\sqrt{E_k(\tilde{\mathbf{q}}(0))}}. \tag{B23}$$

To find the optimal perturbation for time $t = T$, an iterative scheme is performed, which propagates arbitrary initial perturbation in velocity forward in time until time $t = T$, using the direct Eqs. (A11) to (A22). The concentration fields have to admit Eqs. (B19) and (B20). Subsequently, this end state $\mathbf{q}(t = T)$ is used as an initial condition for $\tilde{\mathbf{q}}(t = T)$ [regarding Eq. (B18)], which is propagated backwards using the adjoint equations until time $t = 0$. Relations (B18)–(B20) are enforced directly, but (B23) must be achieved iteratively to reach a stationary value of L. The new initial condition for the direct problem is set by (B23) to start a new loop. The problem has converged when condition (B23) holds up to some error $\epsilon < 10^{-10}$, i.e. the initial conditions only marginally change between iterative loops.

APPENDIX C: THREE-DIMENSIONAL NONLINEAR SIMULATIONS: NUMERICAL METHOD

The numerical code solves the Navier-Stokes-Boussinesq equations and the reaction-diffusion-advection equations. It has been used and described in Ref. [39,40] for interfacial convection in a two-layer systems. However, in contrast to Ref. [39], nonlinear terms are implemented with a first-order Euler forward scheme in order to reduce the demand of main memory. The simulation is performed using the poloidal-toroidal decomposition of the velocity field, whereby incompressibility is automatically satisfied. The dynamical equations for the poloidal and toroidal components and the various concentrations are discretized using a pseudospectral method: Fields are expanded in truncated Fourier series for the horizontal periodic directions x,y and in Chebyshev polynomials for the vertical direction z. Usage of Fourier modes leads to an efficient parallel solution scheme as well as low numerical dissipation.

The smallest wave numbers for the x,y directions are $k_{x0} = 2\pi/l_x$, $k_{y0} = 2\pi/l_y$. The wave-number domain is discretized by the following set of wave numbers:

$$k_x = -\frac{N_x}{2}\frac{2\pi}{l_x},\ldots,\left(\frac{N_x}{2}-1\right)\frac{2\pi}{l_x}, \tag{C1}$$

$$k_y = -\frac{N_y}{2}\frac{2\pi}{l_y},\ldots,\left(\frac{N_y}{2}-1\right)\frac{2\pi}{l_y}. \tag{C2}$$

The data output in physical space and the nonlinear terms are computed at the collocation points,

$$(x_n,y_m,z_k) = \left(nl_x/N_x, ml_y/N_y, \tfrac{1}{2}(1+\cos(k\pi/N_z))\right), \tag{C3}$$

with $n \in [0,1,\ldots,N_x-1]$, $m \in [0,1,\ldots,N_y-1]$, $k \in [0,1,\ldots,N_z]$. The transformation from physical space into wave-number space is partly dealiased by zeroing all Fourier modes corresponding to wave numbers larger or equal to three quarters of the maximum wave number, i.e.,

$$\hat{Q}(k_x,k_y) = 0 \text{ for } |k_x| \geqslant k_{x0}\frac{N_x}{2}\frac{3}{4} \text{ or } |k_y| \geqslant k_{y0}\frac{N_y}{2}\frac{3}{4}. \tag{C4}$$

The number of grid points in each direction is a power of 2 because only base 2 fast Fourier transforms (FFTs) are used. All simulations have a vertical resolution of $N_z = 128$.

We adapt the value of the time step at step $n+1$ to be equal to $\delta t^{n+1} = \min(\delta t_{\max}, \delta t_{\mathrm{CFL}}^{n+1})$ where the value $\delta t_{\max}$ is enforced throughout the study to be $\delta t_{\max} = 5 \times 10^{-3}$. For the calculation of $\delta t_{\mathrm{CFL}}^{n+1}$, the CFL number at time n is calculated as follows:

$$C_g^n = \delta t^n \max\left\{\frac{u_x}{\Delta x},\frac{u_y}{\Delta y},\frac{u_z}{\Delta z}\right\}. \tag{C5}$$

When C_g^n is in the interval

$$C_b/2 \leqslant C_g^n \leqslant C_b, \tag{C6}$$

we set $\delta t_{\mathrm{CFL}}^{n+1} = \delta t_{\mathrm{CFL}}^n$. We have chosen the size of this interval in order to provide a stable numerical scheme by $C_b = 0.15$ but increased it up to $C_b = 0.3$ for times beyond the onset of convection. For the case of having a too-small time step $C_g^n < C_b/2$ (or, respectively, too large, $C_g^n > C_b$), we set $\delta t_{\mathrm{CFL}}^n = C_b \delta t^n / C_g^n$ [respectively, $\delta t_{\mathrm{CFL}}^n = C_b \delta t^n / (2C_g^n)$].

Parallelization with message passing interface (MPI) is based on a domain decomposition in one horizontal direction, which requires transposition of the array of expansion coefficients across the MPI tasks in order to compute the FFTs. For the resolution of $1024 \times 1024 \times 128 \sim 10^8$ the simulations program needs usually 52 Gb of main memory to run. Usually it runs on 128 to 256 MPI processes. The ratio of simulated time to wall-clock time is around 2×10^{-4}, although it clearly changes with flow velocity, generated output, and used hardware. Typically, advancing by $\Delta t = 200$ took around 10 days on 256 MPI processes.

APPENDIX D: POSTPROCESSING

For any field quantity $Q(x,y,z,t)$, we may average over a vertical line,

$$\bar{Q}(x,y,t) \equiv \int_0^1 Q(x,y,z,t)dz, \tag{D1}$$

a horizontal plane,

$$\langle Q\rangle_{xy}(z,t) \equiv \frac{1}{l_x l_y}\int_0^{l_y}\int_0^{l_x} Q(x,y,z,t)dxdy, \tag{D2}$$

or a volume,

$$\langle Q\rangle_{xyz}(t) \equiv \frac{1}{l_x l_y}\int_0^{l_y}\int_0^{l_x}\int_0^1 Q(x,y,z,t)dxdydz. \tag{D3}$$

The length scales in the distribution of Q are quantified by a discrete Fourier analysis of $\bar{Q}(x,y,t)$ computed using its value given at the discrete points x_n, y_m, i.e.,

$$\hat{Q}(k_x,k_y,t) = \frac{1}{N_x N_y}\sum_{n=0}^{N_x-1}\sum_{m=0}^{N_y-1}\bar{Q}(x_n,y_m,t)e^{ik_x x_n}e^{ik_y y_m}, \tag{D4}$$

with the set of wave numbers given in (C2).

From this amplitude, a power spectrum,

$$H_2^Q(k,t) = \sum_{\sqrt{k_x^2+k_y^2}\in[k\pm\frac{\pi}{2}]} |\hat{Q}(k_x,k_y,t)|^2, \tag{D5}$$

is calculated and two dominant wave numbers are identified: a weighted average k_{avg},

$$k_{\mathrm{avg}}^Q(t) = \frac{\sum_k H_2^Q(k,t)k}{\sum_k H_2^Q(k,t)}, \tag{D6}$$

or the wave number $k_{\max}(t)$ for which the power spectrum reaches its maximum at time t,

$$H_2^Q(k_{\max}^Q(t),t) = \max_k H_2^Q(k,t). \tag{D7}$$

Finally, one can also extract from $\bar{Q}(x,y,t)$ its variance

$$\sigma_Q^2(t) = \left\langle Q_{\mathrm{eff}}^2(x,y,t)\right\rangle_{xy}, \text{ with}$$
$$Q_{\mathrm{eff}}(x,y,t) = \bar{Q}(x,y,t) - \langle Q(x,y,z,t)\rangle_{xyz}. \tag{D8}$$

---

[1] P. G. Falkowski, R. T. Barber, and V. Smetacek, Science **281**, 200 (1998).

[2] R. B. Bird, W. E. Stewart, and E. N. Lightfoot, *Transport Phenomena* (John Wiley & Sons, New York, 2007).

[3] J. Ennis-King and L. Paterson, in *Fifth International Conference on Greenhouse Gas Control Technologies, Cairns*, Vol. 1 (CSIRO Publishing, Collingwood, 2001), pp. 290–295.

[4] S. Chandrasekhar, *Hydrodynamic and Hydromagnetic Stability* (Courier Dover, New York, 2013).

[5] C. Sternling and L. Scriven, AIChE J. **5**, 514 (1959).

[6] A. De Wit, K. Eckert, and S. Kalliadasis, Chaos **22**, 037101 (2012).

[7] A. Zalts, C. El Hasi, D. Rubio, A. Urena, and A. D'Onofrio, Phys. Rev. E **77**, 015304 (2008).

[8] C. Almarcha, P. M. Trevelyan, L. A. Riolfo, A. Zalts, C. El Hasi, A. D'Onofrio, and A. De Wit, J. Phys. Chem. Lett. **1**, 752 (2010).

[9] L. Lemaigre, M. Budroni, L. Riolfo, P. Grosfils, and A. De Wit, Phys. Fluids **25**, 014103 (2013).

[10] C. Almarcha, P. M. J. Trevelyan, P. Grosfils, and A. DeWit, Phys. Rev. Lett. **104**, 044501 (2010).

[11] J. D'Herncourt, A. De Wit, and A. Zebib, J. Fluid Mech. **576**, 445 (2007).

[12] A. De Wit, Phys. Fluids **16**, 163 (2004).

[13] D. M. Escala, M. A. Budroni, J. Carballido-Landeira, A. De Wit, and A. P. Munuzuri, J. Phys. Chem. Lett. **5**, 413 (2014).

[14] L. Rongy, P. M. J. Trevelyan, and A. De Wit, Phys. Rev. Lett. **101**, 084503 (2008).

[15] L. Rongy and A. De Wit, Phys. Rev. E **77**, 046310 (2008).

[16] M. Budroni, L. Rongy, and A. De Wit, Phys. Chem. Chem. Phys. **14**, 14619 (2012).

[17] É. Pópity-Tóth, V. Pimienta, D. Horváth, and Á. Tóth, J. Chem. Phys. **139**, 164707 (2013).

[18] K. Eckert and A. Grahn, Phys. Rev. Lett. **82**, 4436 (1999).

[19] K. Eckert, M. Acker, and Y. Shi, Phys. Fluids **16**, 385 (2004).

[20] K. Schwarzenberger, K. Eckert, and S. Odenbach, Chem. Eng. Sci. **68**, 530 (2012).

[21] D. Bratsun and A. De Wit, Chem. Eng. Sci. **66**, 5723 (2011).

[22] M. A. Budroni, L. A. Riolfo, L. Lemaigre, F. Rossi, M. Rustici, and A. De Wit, J. Phys. Chem. Lett. **5**, 875 (2014).

[23] P. Möckel, Naturwissenschaften **64**, 224 (1977).

[24] D. Avnir and M. Kagan, Nature **307**, 717 (1984).

[25] D. Avnir and M. Kagan, Naturwissenschaften **70**, 361 (1983).

[26] D. Avnir and M. Kagan, Chaos **5**, 589 (1995).

[27] A. Pons, F. Sagues, M. Bees, and P. Sørensen, J. Phys. Chem. B **104**, 2251 (2000).

[28] M. Bees, A. Pons, P. G. Sørensen, and F. Sagués, J. Chem. Phys. **114**, 1932 (2001).

[29] A. Pons, F. Sagués, M. Bees, and P. Sørensen, J. Phys. Chem. B **106**, 7252 (2002).

[30] A. J. Pons, F. Sagués, and M. A. Bees, Phys. Rev. E **70**, 066304 (2004).

[31] A. J. Pons, O. Batiste, and M. A. Bees, Phys. Rev. E **78**, 016316 (2008).

[32] F. Doumenc, E. Chénier, B. Trouette, T. Boeck, C. Delcarte, B. Guerrier, and M. Rossi, Int. J. Heat Mass Transf. **63**, 336 (2013).

[33] P. Schmid, Annu. Rev. Fluid Mech. **39**, 129 (2007).

[34] L. Trefethen, A. Trefethen, S. Reddy, T. Driscoll, *et al.*, Science **261**, 578 (1993).

[35] F. Incropera and D. Dewitt, *Fundamentals of Heat and Mass Transfer* (Wiley, New York, 1996).

[36] M. J. Moran, H. N. Shapiro, D. D. Boettner, and M. Bailey, *Fundamentals of Engineering Thermodynamics* (Wiley, New York, 2008).

[37] F. Doumenc, T. Boeck, B. Guerrier, and M. Rossi, J. Fluid Mech. **648**, 521 (2010).

[38] B. Farrell and P. Ioannou, J. Atmos. Sci. **53**, 2041 (1996).

[39] T. Boeck, A. Nepomnyashchy, I. Simanovskii, A. Golovin, L. Braverman, and A. Thess, Phys. Fluids **14**, 3899 (2002).

[40] T. Köllner, K. Schwarzenberger, K. Eckert, and T. Boeck, Phys. Fluids **25**, 092109 (2013).

[41] L. N. Howard, in *Applied Mechanics* (Springer, Berlin, 1966), pp. 1109–1115.

[42] L. Adamcikova, K. Pavlikova, and P. Sevcik, Int. J. Chem. Kinet. **31**, 463 (1999).